JGR Solid Earth

RESEARCH ARTICLE
10.1029/2021JB022618

Transient Creep in Subduction Zones by Long-Range Dislocation Interactions in Olivine

David Wallis[1], Mike Sep[2], and Lars N. Hansen[3]

[1]Department of Earth Sciences, University of Cambridge, Cambridge, UK, [2]Department of Earth Sciences, Utrecht University, Utrecht, The Netherlands, [3]Department of Earth and Environmental Sciences, University of Minnesota, Minneapolis, MN, USA

Key Points:

- Olivine from Oman–UAE ophiolite preserves significant stress heterogeneity imparted by dislocations
- The stress heterogeneity supports a recent model for transient creep based on elastic interactions among dislocations
- The dislocation-interaction model predicts order-of-magnitude changes in mantle viscosity due to earthquake loading

Correspondence to:
D. Wallis,
dw584@cam.ac.uk

Citation:
Wallis, D., Sep, M., & Hansen, L. N. (2022). Transient creep in subduction zones by long-range dislocation interactions in olivine. *Journal of Geophysical Research: Solid Earth*, *127*, e2021JB022618. https://doi.org/10.1029/2021JB022618

Received 16 JUN 2021
Accepted 6 JAN 2022

Author Contributions:
Conceptualization: David Wallis, Mike Sep, Lars N. Hansen
Data curation: David Wallis
Formal analysis: David Wallis, Mike Sep
Funding acquisition: David Wallis
Investigation: David Wallis, Mike Sep
Methodology: David Wallis, Mike Sep, Lars N. Hansen
Project Administration: David Wallis
Resources: David Wallis
Software: David Wallis, Lars N. Hansen
Supervision: David Wallis
Validation: David Wallis
Visualization: David Wallis, Mike Sep
Writing – original draft: David Wallis, Mike Sep
Writing – review & editing: David Wallis, Mike Sep, Lars N. Hansen

Abstract Large earthquakes transfer stress from the shallow lithosphere to the underlying viscoelastic lower crust and upper mantle, inducing transient creep during the postseismic interval. Recent experiments on olivine have provided a new rheological model for this transient creep based on the accumulation and release of back stresses among dislocations. Here, we test whether natural rocks preserve dislocation-induced stress heterogeneity consistent with the back-stress hypothesis by mapping olivine from the palaeosubduction interface of the Oman-UAE ophiolite with high-angular resolution electron backscatter diffraction. The olivine preserves heterogeneous residual stresses that vary in magnitude by several hundred megapascals over length scales of a few micrometers. Large stresses are commonly spatially associated with elevated densities of geometrically necessary dislocations within subgrain interiors. These spatial relationships, along with characteristic probability distributions of the stresses, confirm that the stress heterogeneity is generated by the dislocations and records their long-range elastic interactions. Images of dislocations decorated by oxidation display bands of high and low dislocation density, suggesting that dislocation interactions contributed to the organization of the substructure. These results support the applicability of the back-stress model of transient creep to deformation in the mantle portion of plate-boundary shear zones. The model predicts that rapid stress changes, such as those imposed by large earthquakes, can induce order-of-magnitude changes in viscosity that depend nonlinearly on the stress change, consistent with inferences of mantle rheology from geodetic observations.

Plain Language Summary Large earthquakes are generated in relatively cold and brittle rocks but also change the stresses acting on hotter rocks beneath the fault zone. These stress changes cause flow of the hot rocks in the Earth's upper mantle. Both laboratory experiments and observations of deformation at Earth's surface indicate that the viscosity of mantle rocks typically increases by orders of magnitude over the initial increments of deformation after an earthquake. However, the microscale processes that cause this viscosity evolution remain unclear. Recent laboratory experiments suggest that the viscosity evolution may be caused by elastic interactions among linear defects, dislocations, in the crystal lattice of the mineral olivine. Here, we test the relevance of this model to natural rocks by assessing whether the stresses that generate elastic interactions among dislocations are preserved in rocks from Earth's mantle that have been brought to the surface by the motion of tectonic plates. The new observations reveal significant stresses, imparted by dislocations, within individual grains of olivine. This finding supports the relevance of the laboratory-derived model, which in turn allows the model to be used to predict the magnitude of viscosity changes affecting similar rocks in Earth's mantle.

1. Introduction

Major earthquakes cause near-instantaneous transfer of stress from the shallow lithosphere to the underlying lower crust and/or upper mantle (Campbell & Menegon, 2019; Matysiak & Trepmann, 2012; Muto et al., 2019; Nüchter & Ellis, 2011). These changes in stress state commonly induce periods of rapid viscous flow at a depth that are detectable in geodetic data as surface displacements that decay with distance from the fault and with time after the earthquake (Broerse et al., 2015; Freed et al., 2012; Masuti et al., 2016; Moore et al., 2017; Muto et al., 2019; Savage et al., 2005; Weiss et al., 2019). Modeling of this postseismic creep provides a vital source of information on the evolution of stress states on fault systems (Freed, 2005; Nüchter & Ellis, 2011; Thatcher, 1983) and the rheological properties of the lower crust and upper mantle (Broerse et al., 2015; Freed et al., 2006b, 2012; Masuti et al., 2016; Moore et al., 2017; Muto et al., 2019; Weiss et al., 2019).

The task of modeling postseismic creep is complicated by the complexity of material behavior in response to changes in stress. Most flow laws describing high-temperature creep are formulated and calibrated based on steady-state deformation at constant stress and strain rate attained at strains above a few percent (Hirth & Kohlstedt, 2003). However, laboratory experiments on minerals and many other materials demonstrate that changes in stress induce a period of transient evolution in viscosity (Andrade, 1910; Birch & Wilshire, 1974; Chopra, 1997; De Bresser, 1996; Duval et al., 1983; Gangi, 1983; McLaren et al., 1989; Smith, 1948; Smith & Carpenter, 1987; Wyatt, 1951). Following increases or decreases in applied stress/strain rate, the initial apparent viscosities of olivine, for example, can be up to an order of magnitude lower than those at an eventual steady state (Chopra, 1997; Cooper et al., 2016; Hansen et al., 2021; Hanson & Spetzler, 1994; Post, 1977; Smith & Carpenter, 1987). This transient creep results from microstructural evolution, such as changes in dislocation density and arrangement, in response to the change in stress (Durham et al., 1977; Hanson & Spetzler, 1994). These laboratory observations are mirrored in geodetic data on postseismic creep that can only be adequately fit by models employing transient rheological behaviors with magnitudes of viscosity change comparable to those observed in experiments (Broerse et al., 2015; Freed et al., 2012; Savage et al., 2005).

Due to the complexity of the material behavior and underlying microphysical processes, it is difficult to formulate models of transient creep that can be confidently applied to natural deformation. For olivine, which exerts the dominant control on the viscosity of mantle rocks, many phenomenological models have been compared to experimental data (Chopra, 1997; Hanson & Spetzler, 1994; Post, 1977). However, as the forms of such models are not based on specific microphysical processes, their relevance to natural deformation, occurring under different conditions and potentially by different mechanisms compared to those operating in laboratory experiments, is difficult to verify. One model with a more developed physical basis focuses on stress transfer between two groups of anisotropic grains, one oriented to activate an easy slip system that controls the low initial viscosity, and one in a strong orientation that controls the higher steady-state viscosity (Ashby & Duval, 1985; Karato, 1998; Masuti et al., 2019). This concept has provided the basis for recent formulations of nonlinear adaptations of the classic Burgers model applied to postseismic creep after megathrust earthquakes (Masuti et al., 2016; Muto et al., 2019). These models are generally parameterized based on power-law flow laws for steady-state creep, that is, they assume that the individual crystals are at steady state and the transient results entirely from grain interactions. However, single crystals of olivine deforming by individual slip systems, in which this stress-transfer model cannot apply, also exhibit transient creep over the strain intervals (<1%) relevant to postseismic deformation (Cooper et al., 2016; Durham et al., 1979; Hansen et al., 2021; Hanson & Spetzler, 1994). This effect casts doubt on the relevance of flow-law parameters determined at steady state to the behavior of rocks undergoing transient creep and on the relevance of the stress-transfer model to the low strains at which intragranular processes may dominate the transient behavior (Durham et al., 1977; Hanson & Spetzler, 1994).

A significant development has been the recent formulation of a model for transient creep of olivine based on specific intragranular processes. Mechanical data and microstructural observations from deformation experiments on single crystals and aggregates of olivine at temperatures <600°C indicate that strain hardening during low-temperature plasticity results primarily from long-range elastic interactions among dislocations via their stress fields, termed 'kinematic hardening' (Hansen et al., 2019; Kumamoto et al., 2017; Wallis et al., 2020). These interactions generate back stress that counteracts the applied stress (Bayley et al., 2006; Hansen et al., 2019). Back stress can be generated when dislocations pile up against obstacles that block their slip plane, but can also arise from more complex arrangements of dislocations (Wallis et al., 2020). Notably, the interactions are recorded in the experimental samples as heterogeneous residual stresses, measured by high-angular resolution electron backscatter diffraction (HR-EBSD), that vary in magnitude on the order of 1 GPa over distances of a few micrometers (Wallis et al., 2020). Wallis, Hansen, et al. (2021) made a detailed comparison of intragranular stress heterogeneity in samples deformed at room temperature and samples deformed at 1150–1250°C by power-law creep. The residual stresses within the two sets of samples were essentially indistinguishable and were demonstrated to be long-range internal stresses (i.e., acting over distances greater than the average dislocation spacing) generated by dislocations in both cases. These similarities suggest that long-range dislocation interactions likely also contribute to transient creep at high temperatures (Wallis, Hansen, et al., 2021). This hypothesis has been verified by recent stress-reduction experiments on single crystals of olivine at temperatures of 1250–1300°C (Hansen et al., 2021). When sufficiently large reductions in stress are imposed during creep, the samples undergo time-dependent reverse strain. This behavior can also be well modeled using the flow-law for dislocation glide initially formulated for low-temperature plasticity, with the reverse strain being generated when the dislocation-induced back stress exceeds the

applied stress (Hansen et al., 2021). Most recently, Thom et al. (2020) performed analogous experiments at room temperature using nanoindentation and demonstrated that back stress depends on the density of geometrically necessary dislocations in a manner (following the Taylor equation) that is broadly consistent across the low- and high-temperature regimes. However, despite these significant recent advances based on laboratory experiments, a crucial outstanding question remains. Do natural rocks preserve microstructural and micromechanical evidence that is consistent with the back-stress model of transient creep?

Here, we assess the relevance of the back-stress model to natural deformation. Specifically, we test the hypothesis that long-range stress heterogeneity generated by dislocations is preserved in natural samples. This stress heterogeneity is the physical manifestation of the back stress, which arises from it as an emergent property (Hansen et al., 2021; Wallis et al., 2020). We do not aim to characterize all processes that potentially generate transient creep but rather test for evidence that this specific mechanism makes a contribution. We note also that the final increment of deformation to have affected the rocks does not necessarily need to have occurred during a transient for the preserved microstructure to provide information on the mechanisms of transient creep. The statistical characteristics of microstructures and internal stress fields that persist during steady-state creep are necessarily the end products of processes that operated during a preceding transient evolution toward steady state and therefore pertain to those processes (Hansen et al., 2021; Hanson & Spetzler, 1994; Holtzman et al., 2018; Orlová et al., 1972; Orlová & Čadek, 1986; Wallis et al., 2020; Wallis, Hansen, et al., 2021; Weckert & Blum, 1985). Therefore, our primary interest is simply to characterize the stress fields of dislocations that arise in natural rocks and thereby test for the presence of long-range internal stress heterogeneity that would be consistent with the back-stress model of kinematic hardening. We assess the types, densities, and distributions of dislocations in the palaeosubduction interface of the Oman-UAE ophiolite and map intragranular stress heterogeneity using HR-EBSD (Wallis et al., 2019). We analyze the spatial and probability distributions of the stress heterogeneity to test whether it indeed represents long-range internal stress generated by the dislocations. The results provide new constraints on the microphysical processes contributing to transient creep of the upper mantle and allow new predictions of viscosity changes induced by earthquake loading.

2. Methods

2.1. Sample Selection

We focus on samples from the exceptionally well-preserved palaeosubduction interface of the Oman-UAE ophiolite. The oceanic lithosphere of the ophiolite formed in the hanging wall of a newly initiated intraoceanic subduction zone at ca. 96.4–95.5 Ma (MacLeod et al., 2013; Rioux et al., 2016). The Semail thrust forms the lower boundary of the peridotite portion of the ophiolite and represents the palaeosubduction interface (Ambrose et al., 2018; Prigent et al., 2018a, 2018b; Searle & Malpas, 1980). This structure juxtaposes the peridotites, representing the former mantle wedge, with the metamorphic sole, consisting of accreted slices from the downgoing plate (Agard et al., 2016; Ambrose et al., 2018; Prigent et al., 2018a, 2018b; Searle & Malpas, 1980). The conditions of deformation along the Semail thrust are constrained by peak metamorphic temperatures of 770–900°C and pressures of 1.1–1.3 GPa determined from garnet-clinopyroxene amphibolites in the metamorphic sole (Cowan et al., 2014). These conditions are consistent with temperatures in the range 650–850°C determined from mylonitic peridotites in the hanging wall across several massifs of the ophiolite (Prigent, Agard, et al., 2018). The Semail thrust has been uplifted by deeper thrust stacking of underlying (meta)sedimentary units without itself being reactivated at lower temperatures (Searle & Malpas, 1980). Therefore, the structures and microstructures of the basal peridotites were formed during simultaneous deformation and cooling but are largely unaffected by subsequent annealing or deformation during emplacement onto the continental margin (Prigent, Agard, et al., 2018; Searle & Malpas, 1980). This history makes the base of the Oman-UAE ophiolite especially well suited to the study of subduction-zone processes that occurred at depths of approximately 35–40 km.

We utilize samples of peridotite collected and initially analyzed by Ambrose et al. (2018) from the Khor Fakkan block of the ophiolite in the United Arab Emirates. Figure 1 marks the location of the samples on the western edge of the Masafi window. Here, the ophiolite is gently folded, exposing a section through the peridotite and Semail thrust into the underlying sole. Due to this folding, the Semail thrust has an apparent normal shear sense at this location. The sample-set forms a transect extending over a horizontal distance of approximately 900 m from the Semail thrust into the peridotite, corresponding to a structural distance of approximately 500 m normal to the

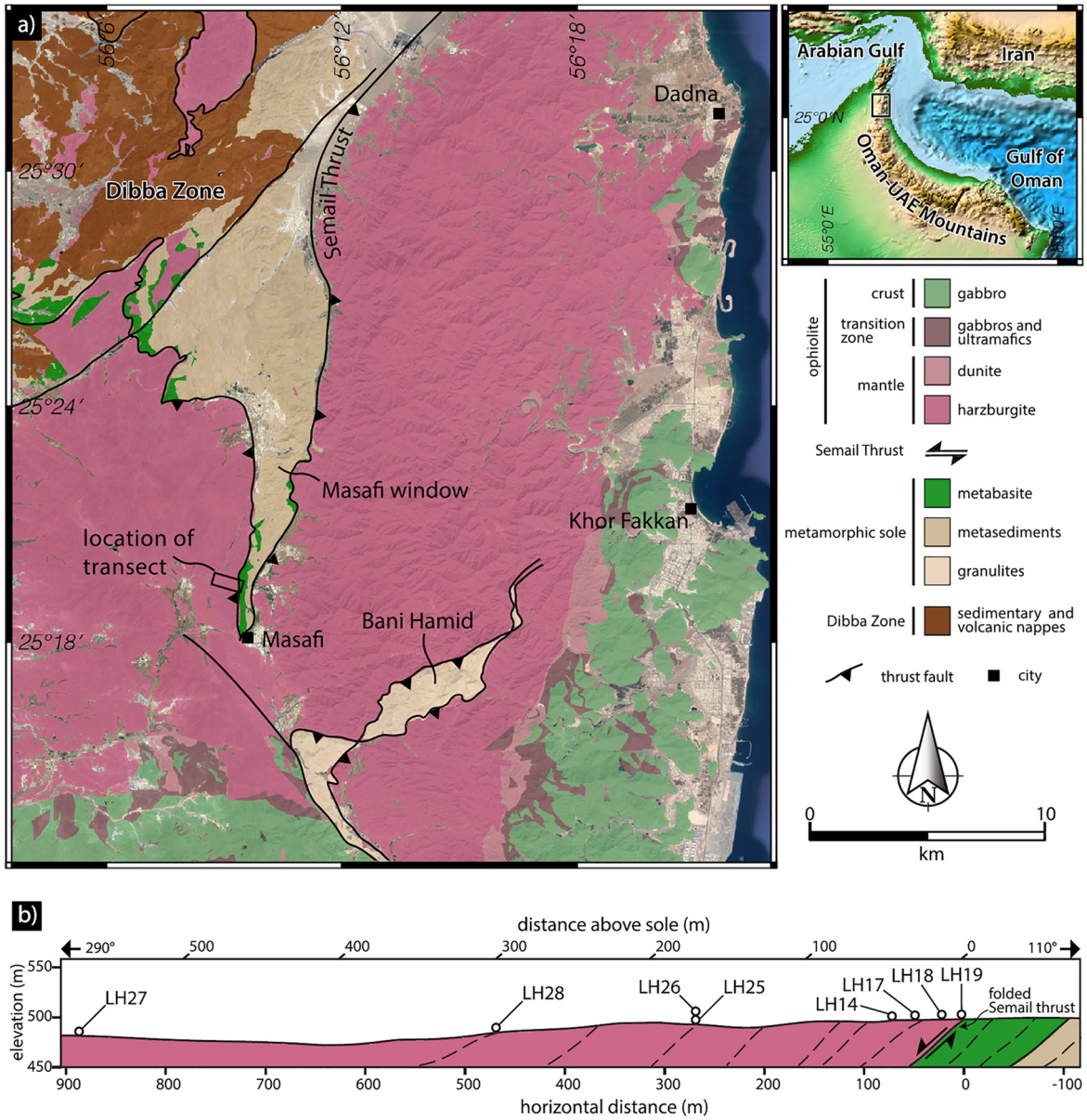

Figure 1. Overview of the field area and sample locations reproduced from Ambrose et al. (2018). (a) Simplified geological map of the northern Oman-UAE mountains modified after Farrant et al. (2012). The inset provides an elevation model with the black box indicating the location of the main map. (b) Cross-section across the uppermost sole and basal peridotites with the locations of samples analyzed by Ambrose et al. (2018). Solid black lines mark lithological contacts, including the Semail thrust, and dashed lines indicate the foliation. Distance above the sole was estimated using the dip of the average foliation of the upper sole and banding in peridotites, which approximate the orientation of the thrust contact. Horizontal distance is taken from the sole-peridotite contact.

thrust plane. The transect samples the mylonitic shear zone, typically <500 m thick, that ubiquitously forms the base of the peridotites (Prigent, Agard, et al., 2018; Searle & Malpas, 1980).

Ambrose et al. (2018) conducted a detailed microstructural study of 8 samples in this transect, which consist of partially serpentinized protomylonitic to ultramylonitic harzburgites. Using electron backscatter diffraction (EBSD), they measured subgrain sizes on the order of 50 μm throughout the transect. These subgrain sizes correspond to macroscopic differential stresses of approximately 20 MPa based on a recent paleopiezometer calibrated using EBSD (Goddard et al., 2020). The grain sizes of olivine are on the order of a few hundred micrometers and decrease toward the contact with the metamorphic sole (Ambrose et al., 2018). The decrease in grain size coincides with an increase in the abundance of secondary phases (e.g., pyroxenes and amphibole) following a Zener

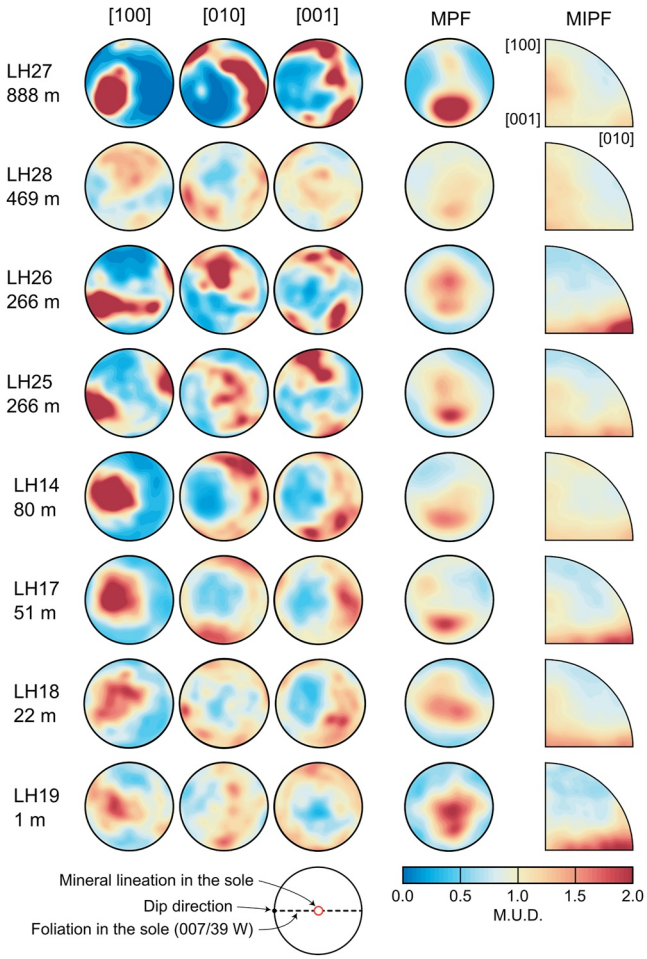

Figure 2. Orientation and misorientation data from conventional electron backscatter diffraction. Pole figures of [100], [010], and [001] present crystal directions in the reference frame aligned with the foliation and lineation of the adjacent metamorphic sole as indicated below. Misorientation pole figures (MPF) present misorientation axes of subgrain boundaries associated with misorientation angles in the range 2–10° and in the same reference frame as the pole figures. Misorientation inverse pole figures (MIPF) present the same misorientation axes in the crystal reference frame. Annotations provide sample numbers and horizontal distances to the contact with the metamorphic sole. M.U.D. indicates multiples of uniform distribution. Pole figures are replotted from Ambrose et al. (2018).

pinning relationship (Ambrose et al., 2018). Grain size also correlates positively with the strength of the crystallographic preferred orientation (CPO) in olivine (Ambrose et al., 2018). Following the established nomenclature (Jung et al., 2006), the CPOs, reproduced in Figure 2, appear to include both B-type (samples LH17 and LH18) and E-type (sample LH25) CPOs if the shear direction is assumed to be parallel to the present dip direction of the foliation and Semail thrust. However, this interpretation is complicated by the presence of a strike-parallel lineation defined by aligned amphibole and elongated plagioclase in the adjacent sole at this locality, which indicates potentially more complex kinematics than simple shear (Ambrose et al., 2018). E-type CPOs are common elsewhere along the base of the peridotite (Prigent, Guillot, et al., 2018) and in structurally higher shear zones formed at similar temperatures (Linckens et al., 2011; Michibayashi & Mainprice, 2004). The remaining CPOs in Figure 2 are difficult to classify. Flow laws for olivine predict that both diffusion and dislocation creep contributed significantly to the total strain rate (54%–97% and 3%–46%, respectively) in the samples of Ambrose et al. (2018). The existing detailed characterization of these samples, along with their record of deformation in the central portion of a palaeosubduction interface, makes them an ideal test case for potential evidence of kinematic hardening in olivine.

We progressively focus our analysis of the intragranular structures in olivine on the most appropriate samples. To test for commonality in the general characteristics of the substructure, we conduct intragranular misorientation analysis on all eight samples investigated using conventional EBSD by Ambrose et al. (2018). To image the distributions of dislocations using oxidation decoration, we focus on three of the least serpentinized samples (LH17, LH18, and LH28), spanning distances of 22–469 m from the sole. To map densities of geometrically necessary dislocations and intragranular stress heterogeneity using HR-EBSD, we made multiple new maps from the least serpentinized sample (LH17, 51 m from the sole), which had an indexing rate of 90% (averaged across all phases) in the conventional EBSD data of Ambrose et al. (2018).

2.2. Sample Preparation

Data were collected on thin sections of samples LH14 and LH19 and billets of all other samples. As the hand samples contained no visible lineation, sections were cut parallel to the dip direction and normal to the strike of the foliation (007/39 W) in the adjacent metamorphic sole. This plane likely approximates the conventional plane of the section containing the shear-plane normal and shear direction during top-to-west thrusting. All specimens were polished with progressively finer diamond slurry from 30 to 0.25 μm and finished with either 0.05 μm diamond or 0.03 μm colloidal silica.

2.3. Conventional EBSD

Conventional EBSD data were collected from all eight samples by Ambrose et al. (2018), who provide full details of the acquisition and processing. Sample LH19 was mapped with a step size of 15 μm and all other samples were mapped with a step size of 5 μm. Olivine was indexed at 15%–68% of the data points, whilst 10%–81% of the data points remained unindexed and were attributed primarily to the presence of serpentine.

2.4. High-Angular Resolution Electron Backscatter Diffraction

For HR-EBSD analysis, we collected four new EBSD datasets from sample LH17 on a Philips XL-30 field emission gun scanning electron microscope at Utrecht University. The specimen surface was coated with 0.5 nm Pt/Pd to reduce charging. The microscope was calibrated for HR-EBSD following Wilkinson et al. (2006) and reference-frame conventions were validated following Britton et al. (2016). Diffraction patterns were acquired at an accelerating voltage of 30 kV and a working distance of 15 mm using an Oxford Instruments NordlysNano EBSD detector and AZtec 3.3 acquisition software. No gain or binning were applied to the 1344 × 1024 pixels in the diffraction patterns, which were saved as 8 bit TIFF files for subsequent HR-EBSD postprocessing. To characterize the substructure and micromechanical state across a range of length scales, the maps (Maps 1–4) were acquired with progressively finer step sizes of 2 μm, 0.6 μm, 0.6 μm, and 0.2 μm, respectively. Map 4 provides a detailed subregion from the same grain as Map 1. All maps for HR-EBSD were positioned within individual grains. The olivine in Map 1 is dissected by bands of serpentine, which were not indexed during data acquisition. The olivine in Map 3 contains two scratches. Data points affected by the scratches were removed from the dataset.

Densities of geometrically necessary dislocations (GNDs) and residual stress heterogeneities were calculated respectively from lattice rotations and elastic strains measured by the HR-EBSD postprocessing method of Wilkinson et al. (2006) and Britton & Wilkinson (2012, 2011). Wallis et al. (2019) provide a comprehensive overview of the application of this technique to geological materials. The cross-correlation procedure maps the shifts in 100 regions of interest within the diffraction patterns relative to their positions in a reference pattern within each grain to overdetermine the deformation gradient tensor describing lattice rotations and elastic strains. For all HR-EBSD maps presented here, the coordinate axes are defined such that axis 1 is horizontal, axis 2 is vertical, and axis 3 is out of the plane of the map. Densities of GNDs were calculated from the rotation fields following the method of Wallis et al. (2016). In this approach, the dislocation types are distinguished by their differing contributions to the components of lattice curvature described by the Nye tensor (Wallis et al., 2016, 2019). Stress heterogeneities were calculated from the elastic-strain heterogeneities using Hooke's law and the elastic constants for olivine at room temperature and confining pressure of 1 atm (Abramson et al., 1997). Reference points were chosen within regions of high pattern quality. It is likely that no portion of this sample is free from elastic strain, and therefore measured strains/stresses are relative to the strain/stress state at the reference point. Therefore, the stress data were normalized by subtracting the mean of each component of the measured stress tensors (σ_{ij}) within the map area, providing maps of relative stress heterogeneity (Jiang et al., 2013; Wallis et al., 2019). Due to large lattice rotations present in Map 1, we considered this dataset to be prone to erroneous 'phantom strains' (Britton & Wilkinson, 2012) and therefore do not further consider the stress data from this map. However, Map 4 provides stress data from a smaller region within the same grain.

For comparison to the new HR-EBSD data from sample LH17, we employ an existing dataset collected on an undeformed Si wafer to act as a control. This dataset was collected by Wallis et al. (2016) and consists of 100 × 100 data points at a step size of 0.25 μm. This sample is free of dislocations and other lattice distortion and therefore characterizes the distribution of noise in the stress measurements.

2.5. Oxidation Decoration

For the present study, we extracted portions of the polished billets of samples LH17, LH18, and LH28 after collection of all EBSD and HR-EBSD data. These portions of the samples were decorated by oxidation following the procedure of Kohlstedt et al. (1976). The samples were oxidized at a temperature of 900°C in air for 45 min. The oxidized surface rind was removed by polishing with colloidal silica for approximately 10 min, exposing fresh olivine containing oxidized dislocations. The polished surfaces were coated with 7 nm Pt/Pd to reduce charging. The decorated dislocations were imaged using backscattered electrons in a FEI Helios Nanolab G3 Dualbeam focused ion beam scanning electron microscope at Utrecht University. Images were obtained at an accelerating voltage of 20 kV and beam current of 3.2 nA. The contrast of the saved images was optimized to emphasise the oxidized dislocations.

2.6. Analysis of Stress Distributions

To interrogate the probability distributions of intragranular stress heterogeneity, we present the σ_{12} data from Maps 2–4 and the Si control dataset on a normal probability plot, in which the vertical axis is scaled such that a

normal distribution falls on a straight line (Jiang et al., 2013; Wilkinson et al., 2014). Departures from a straight line indicate departures from a normal distribution. Work on Cu, InAlN, and steel has demonstrated that samples containing dislocations often exhibit departures from normal distributions to greater stress magnitudes (Jiang et al., 2013; Wilkinson et al., 2014). Recently, Wallis, Hansen, et al. (2021) demonstrated that this effect also occurs in olivine deformed by dislocation-mediated mechanisms at both room temperature and 1150–1250°C. Although the analyses outlined in this section can be performed on any component of σ_{ij} with similar results, we focus our analysis on σ_{12} as this component of the stress tensor is modified least by relaxation during sectioning of the sample (Wallis et al., 2019). This component would also correspond to the shear stresses acting on the macroscopic shear plane in the shear direction if they were aligned with the foliation and its dip direction, respectively.

A remarkable property of the probability distribution, $P(\sigma)$, of the stress field of a population of dislocations is that the high-stress portion, corresponding to the high-stress 'tails' on a normal probability plot, has a particular form. Regardless of their spatial configuration, the probability distribution of the stress field of a population of straight, parallel dislocations tends to $P(\sigma) \propto |\sigma|^{-3}$ at high stresses following

$$P(\sigma) \rightarrow C\rho|\sigma|^{-3}, \tag{1}$$

where C is a constant that depends on the material, type of dislocation, and considered a component of the stress tensor, and ρ is the dislocation density (Csikor & Groma, 2004; Groma & Bakó, 1998; Kalácska et al., 2017; Wilkinson et al., 2014). The extent to which a stress distribution is consistent with this form can be assessed through calculation of the restricted second moment, v_2. This metric characterizes the shape of a probability distribution based on the integral over restricted ranges in stress (Wilkinson et al., 2014), calculated as

$$v_2(\sigma) = \int_{-\sigma}^{+\sigma} P(\sigma)\sigma^2 d\sigma \tag{2}$$

Importantly, a plot v_2 of versus the logarithm of normalized σ_{12} becomes a straight line at high stresses if the stress field exhibits the $P(\sigma) \propto |\sigma|^{-3}$ form expected of a population of dislocations (Kalácska et al., 2017; Wilkinson et al., 2014). Wallis, Hansen, et al. (2021) demonstrated that the stress fields within olivine deformed experimentally at room temperature and 1150–1250°C do indeed exhibit this form. Therefore, we plot the restricted second moment of the σ_{12} distributions from Maps 2–4 and the Si control to test whether the intragranular stress heterogeneity in sample LH17 has the particular form that is characteristic of stresses generated by a population of dislocations. This analysis distinguishes stress heterogeneity imparted by dislocations from that generated by other causes, such as changes in pressure and temperature or mineral reactions, which are unlikely to generate stress distributions that exhibit this particular form.

3. Results

3.1. Misorientation Analysis From Conventional Electron Backscatter Diffraction

Figure 2 presents the misorientation axes of subgrain boundaries in olivine with misorientation angles in the range 2–10°. The misorientation pole figures (MPFs) plot the misorientation axes in a reference frame defined by the foliation and lineation of the metamorphic sole. All samples exhibit a maximum density of misorientation axes in the plane normal to the dip direction of the foliation. This maximum is either approximately parallel to the lineation (e.g., sample LH19) or positioned approximately 45° between the lineation and the normal to the foliation (e.g., sample LH17).

The misorientation inverse pole figures (MIPFs) plot the misorientation axes in the crystal reference frame. All samples, except LH28, exhibit a density maximum of misorientation axes parallel to [010], with lower densities extending across the (100) plane toward [001]. The two samples furthest from the metamorphic sole (LH27 and LH28) exhibit density maxima centered within the (010) plane.

3.2. Decorated Dislocations

Figure 3 presents backscattered electron images of decorated dislocations in olivine in samples LH17, LH18, and LH28. Several characteristics of the dislocations are common among the three samples. Multiple types of dislocation are evident within each grain as either dots or lines of varying orientations. Dislocations that occupy

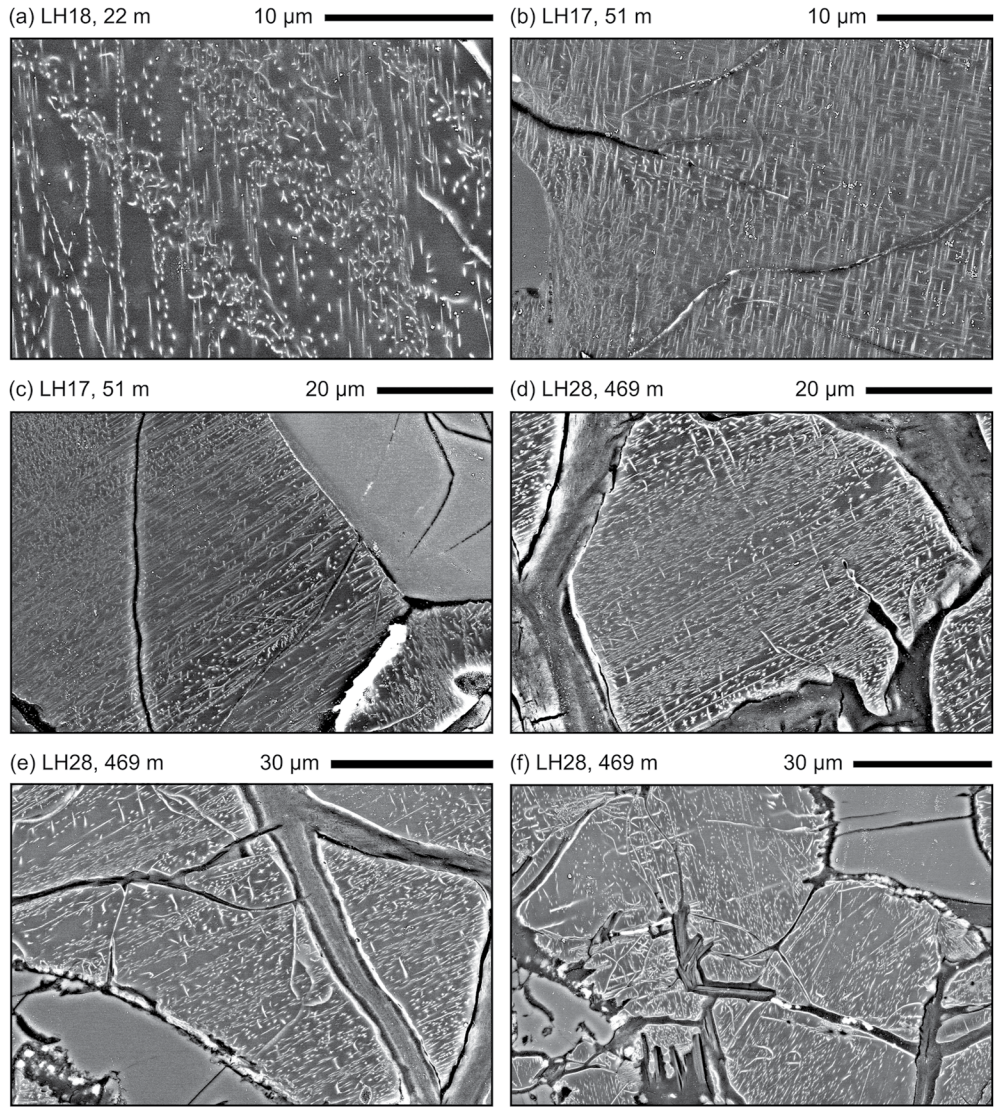

Figure 3. Backscattered electron images of dislocations in olivine decorated by oxidation. Annotations indicate sample number and horizontal distance from the metamorphic sole.

orientations at low angles to the specimen surface are typically straight (e.g., Figures 3a–3c) with occasional sharp angular links (Figure 3b). Significant curvature of the dislocations is only evident in some grains within sample LH28 (Figure 3f), in which the curved dislocations form tangled networks. Several grains contain subgrain boundaries identifiable as linear arrays of closely packed dislocations (e.g., Figures 3a and 3d). The dislocation densities in all samples are heterogeneous and the dislocations are commonly arranged into prominent bands with higher and lower densities alternating over length scales up to approximately 10 μm (Figures 3a, 3d, and 3e). Average dislocation densities are approximately 10^{12} m^{-2} in each sample, but densities vary by up to an order of magnitude between bands within individual grains (Figures 3a, 3d, and 3e).

3.3. High-Angular Resolution Electron Backscatter Diffraction

Figure 4 presents the densities of each type of GND in the HR-EBSD results from Map 1 of sample LH17. Although the grain is dissected by bands of serpentine (white), several subvertical bands of high GND density, on the order of 10^{13} m^{-2}, can be traced across the grain. These bands of high GND density are most evident in the maps of (001)[100] edge dislocations, [100] screw dislocations, and to a lesser extent (010)[100] edge dislocations. The traces of these bands are approximately perpendicular to the [100] axis, which lies close to the plane

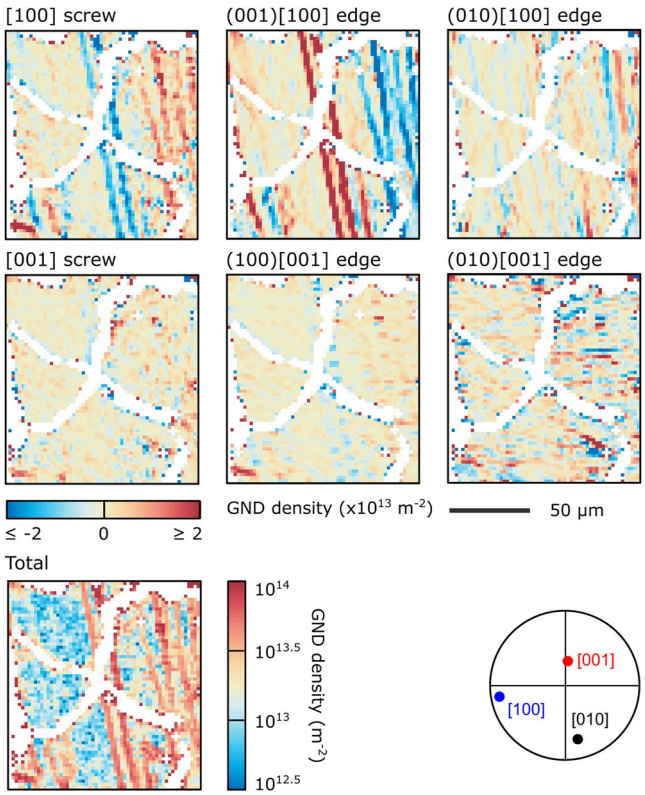

Figure 4. High-angular resolution electron backscatter diffraction (HR-EBSD) data from sample LH17, Map 1. Maps present densities of geometrically necessary dislocations with positive and negative densities indicating dislocations with opposite senses of Burgers vector. White areas indicate pixels that did not index in the original EBSD map or that failed the quality criteria of Britton and Wilkinson (2011) for the cross-correlation analysis. The pole figure indicates the measured crystal orientation.

of the map. This orientation, along with their high GND densities, indicates that these bands are subgrain boundaries.

Figure 5a presents the densities of each type of GND in the HR-EBSD results from Map 2 of sample LH17. This map is also transected by bands of elevated dislocation densities on the order of 10^{13} m^{-2}. However, these bands are evident in maps of several different dislocation types. Unlike Map 1, Map 2 exhibits significant densities of GNDs with [001] Burgers vectors. In particular, a prominent band of (100)[001] edge dislocations crosses the map from top-right to bottom-left. The traces of all structures in the GND maps are parallel to the [001] axis and perpendicular to the [100] axis, both of which lie close to the plane of the map. These orientation relationships suggest that structures containing GNDs with [100] Burgers vectors are likely subgrain boundaries, as in Map 1, whereas GNDs with [001] Burgers vectors occupy slip-band configurations.

Figure 5b presents maps of intragranular stress heterogeneity for each in-plane component of the stress tensor in Map 2. Each map exhibits significant stress heterogeneity with spatial distributions broadly comparable to the maps of GND density in Figure 5a. These heterogeneities are on the order of a few hundred megapascals in magnitude and occur over length scales of a few micrometers. The regions with greater magnitudes of σ_{11} and σ_{22} are collocated with the straighter, narrower bands of elevated GND density that likely represent subgrain boundaries. In contrast, regions with greater magnitudes of σ_{12} correspond most closely with bands of elevated densities of (100)[001] edge dislocations that occupy slip-band orientations (e.g., the band running from top-right to lower-left across the center of the map).

Figure 6a presents the densities of each type of GND in the HR-EBSD results from Map 3 of sample LH17. Similar to Map 2, this map contains bands of (100)[001] edge dislocations aligned with the trace of the (100) plane, suggesting that they are slip bands. These bands coincide with bands (010)[001] edge dislocations, which cannot be rationalized as slip bands or tilt walls due to their alignment with the trace of the (100) plane. As with Maps 1 and 2, total GND densities in these bands are on the order of 10^{13} m^{-2}.

Figure 6b presents maps of intragranular stress heterogeneity for each in-plane component of the stress tensor in Map 3. Again, similar to Map 2, the bands of elevated GND density coincide with elevated residual stresses. The σ_{11} and σ_{22} components reach approximately 300 MPa in magnitude, whereas the σ_{12} component reaches approximately 200 MPa. Areas of the elevated residual stress of consistent sign stretch the full length of the bands of elevated GND density and up to a few micrometers perpendicular to the bands.

Figure 7a presents the densities of each type of GND in the HR-EBSD results from Map 4 of sample LH17. The map is bisected by a band of high densities, $>10^{14}$ m^{-2}, of predominantly (001)[100] edge dislocations. The trace of this band is perpendicular to the [100] axis, indicating that this structure is a subgrain boundary with the same characteristics as those in Map 1. The GND content of the adjacent subgrain interiors is remarkably different on either side of the boundary. Elevated densities of (001)[100] and (010)[100] edge dislocations are present to the left of the boundary. Both types of dislocation occur in two subvertical swathes dominated by dislocations with opposite senses of Burgers vector (indicated by red and blue in the maps) corresponding to opposite senses of lattice curvature. To the left of the boundary, GND densities approach 10^{14} m^{-2}. In contrast, to the right of the boundary, GND densities are lower, $<5 \times 10^{13}$ m^{-2}, and more homogeneous.

Figure 7b presents maps of intragranular stress heterogeneity across the same area as Figure 7a. To the left of the subgrain boundary, each component of the stress tensor varies smoothly in a manner that reflects the structure evident in the maps of GND density. Similar to those in Figures 5b and 6b, the stresses vary in magnitude by several hundred megapascals over distances of approximately 2 μm. A region of elevated shear stress, σ_{12}, is collocated with high GND densities adjacent to the subgrain boundary. Each component of the stress tensor changes

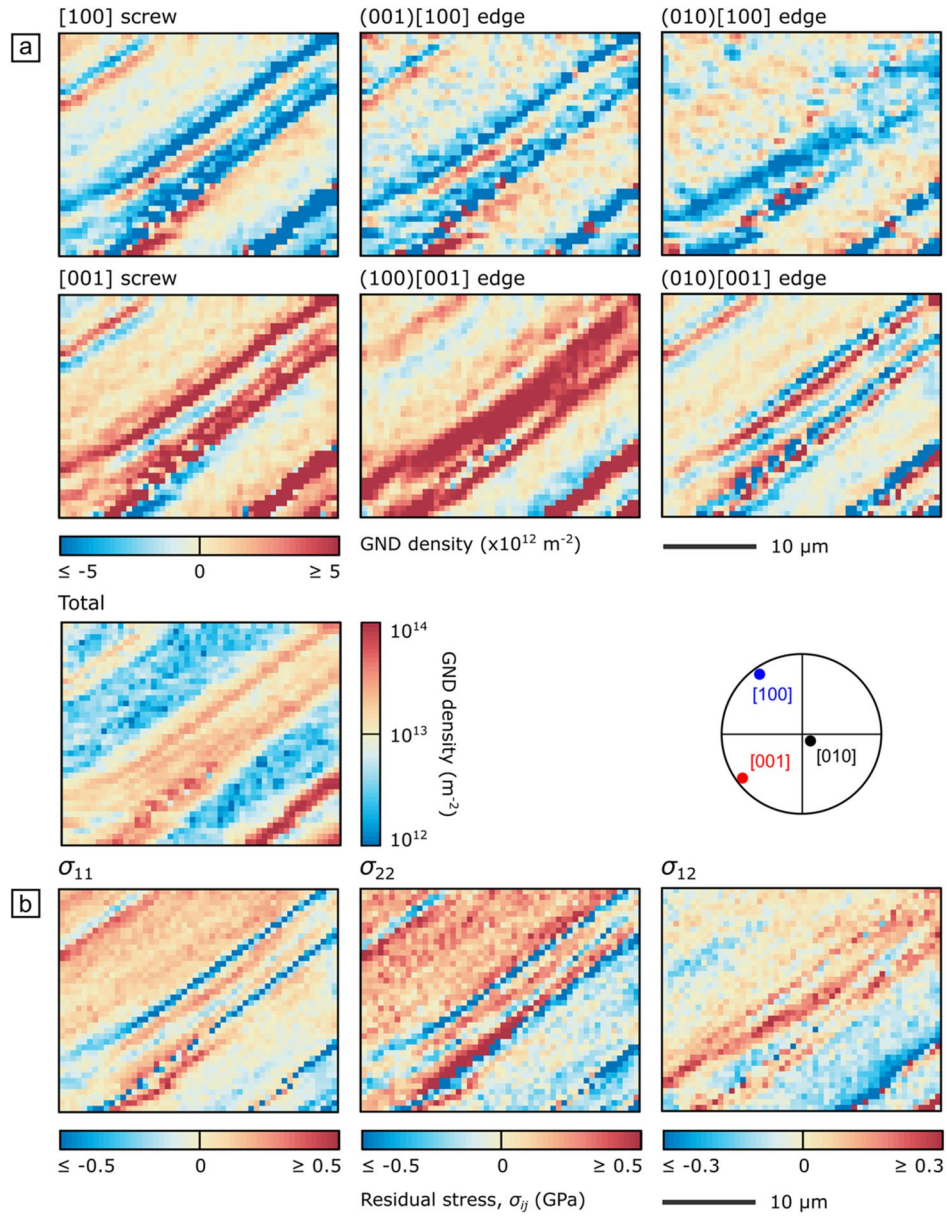

Figure 5. High-angular resolution electron backscatter diffraction data from sample LH17, Map 2. (a) Densities of geometrically necessary dislocations. Positive and negative densities indicate dislocations with opposite senses of Burgers vector. The pole figure indicates the measured crystal orientation. (b) Stress heterogeneity is relative to the mean of each component of the stress tensor (σ_{ij}) within the map area.

in magnitude abruptly across the subgrain boundary and the stress state is more homogeneous to the right of the boundary.

3.4. Analysis of Stress Distributions

Figure 8 characterizes the probability distributions of intragranular heterogeneity in σ_{12} from Maps 2–4 of sample LH17 and the Si control dataset. Figure 8a presents the data on a normal probability plot. The Si data have a standard deviation of 22 MPa and lie on a straight line that indicates a normal distribution, as expected of measurement noise. In contrast, the data from Maps 2–4 have standard deviations of 117 MPa, 77 MPa, and 385 MPa, respectively, and only follow straight lines at magnitudes less than approximately 150 MPa. At greater stress magnitudes, the probability distributions depart from straight lines, indicating departures from normal distributions.

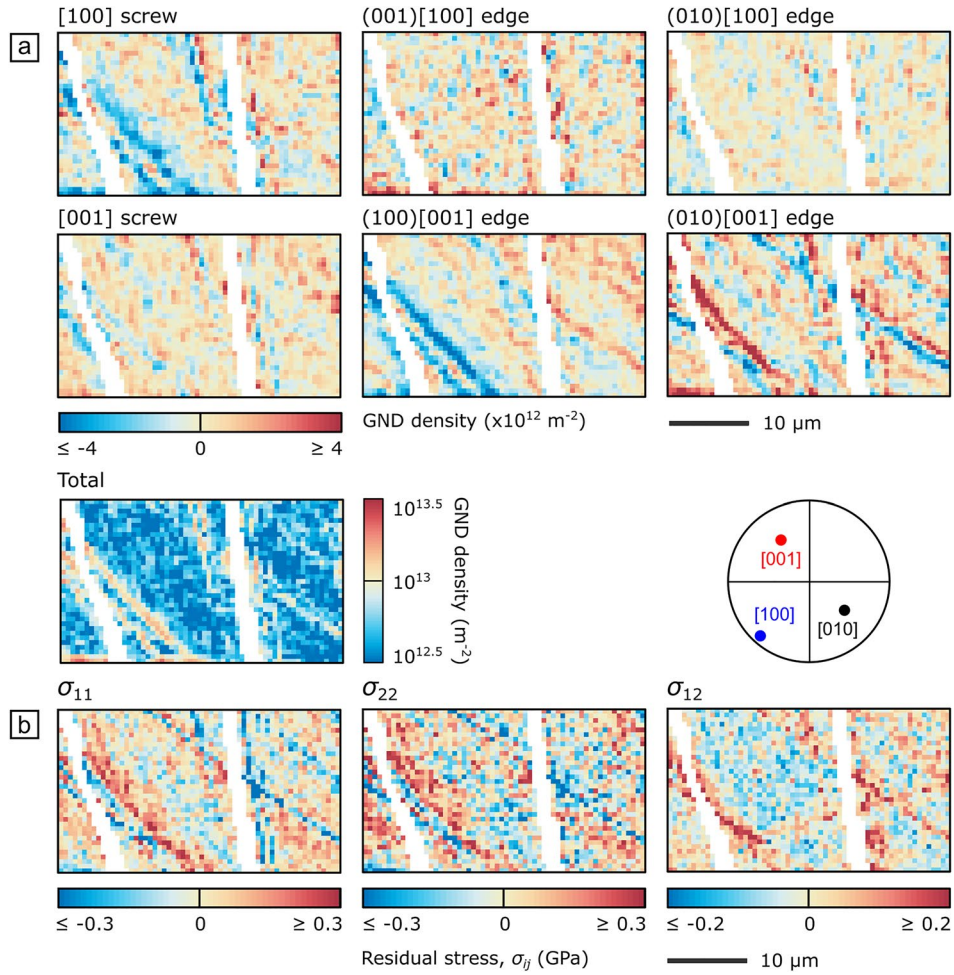

Figure 6. High-angular resolution electron backscatter diffraction data from sample LH17, Map 3. (a) Densities of geometrically necessary dislocations. Positive and negative densities indicate dislocations with opposite senses of Burgers vector. The pole figure indicates the measured crystal orientation. (b) Stress heterogeneity is relative to the mean of each component of the stress tensor (σ_{ij}) within the map area. White regions mark scratches.

Figure 8b presents the restricted second moment, ν_2, as a function of $\ln(\sigma_{12})$ for Maps 2–4 of sample LH17 and the Si control. The data from LH17 extend to greater stress magnitudes and values of ν_2, than those of the control dataset. Importantly, these high-stress data fall on straight lines at stresses greater than approximately 200 MPa. The data from Map 2 depart slightly from the straight line at stresses >650 MPa.

4. Discussion

4.1. Characteristics and Origins of Dislocation Structures

The EBSD and HR-EBSD results reveal diverse evidence of dislocation activity. Each sample exhibits a pronounced CPO (Figure 2), consistent with predictions of flow laws suggesting that dislocation creeps contributed up to approximately 50% of the total strain rate (Ambrose et al., 2018). However, it is difficult to reconcile strike-parallel misorientation axes (Figure 2) with the strike-parallel lineation in the adjacent metamorphic sole (Ambrose et al., 2018) into a simple kinematic model, which makes it challenging to classify the CPO types and interpret associated slip systems. Nonetheless, the misorientation analyses from EBSD and GND densities from HR-EBSD provide detailed additional information on the types of dislocations that were active.

The misorientation inverse pole figures (Figure 2) constrain the dominant dislocation types contributing to subgrain boundaries across the large map areas (up to approximately 1 cm across) of the conventional EBSD data

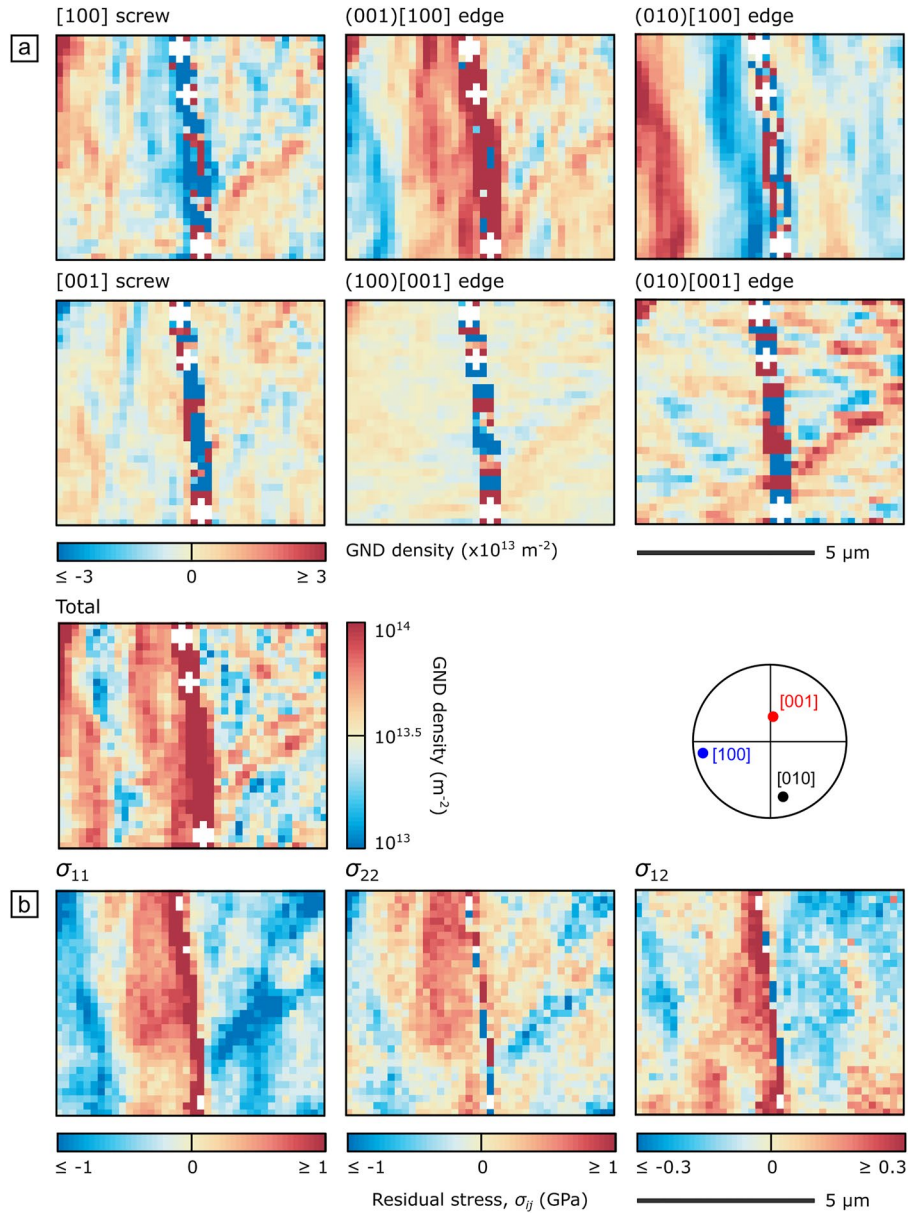

Figure 7. High-angular resolution electron backscatter diffraction data from sample LH17, Map 3. (a) Densities of geometrically necessary dislocations. Positive and negative densities indicate dislocations with opposite senses of Burgers vector. The pole figure indicates the measured crystal orientation. (b) Stress heterogeneity is relative to the mean of each component of the stress tensor (σ_{ij}) within the map area. White areas indicate pixels that failed the quality criteria of Britton and Wilkinson (2011) for the cross-correlation analysis.

of Ambrose et al. (2018). The misorientation axes are primarily approximately parallel to [010] with a subpopulation forming a girdle in the misorientation inverse pole figures extending toward [001] (Figure 2). Misorientation axes parallel to [010] indicate the presence of either tilt walls composed of (001)[100] or (100)[001] edge dislocations or twist boundaries composed of screw dislocations with [100] and [001] Burgers vectors (de Kloe et al., 2002). Misorientation axes parallel to [001] indicate the presence of tilt boundaries composed of (010)[100] edge dislocations (de Kloe et al., 2002). The distributions of misorientation axes in both the crystal and sample reference frames are broadly consistent across the sample set (Figure 2), which suggests that the dislocation content of the samples analyzed in more detail by HR-EBSD and oxidation decoration are representative of the wider transect. These observations are also consistent with the misorientation analyses of Prigent, Guillot, et al. (2018), who analyzed samples from the basal peridotites across the Khawr Fakkan, Fizh, Haylayn, Wadi

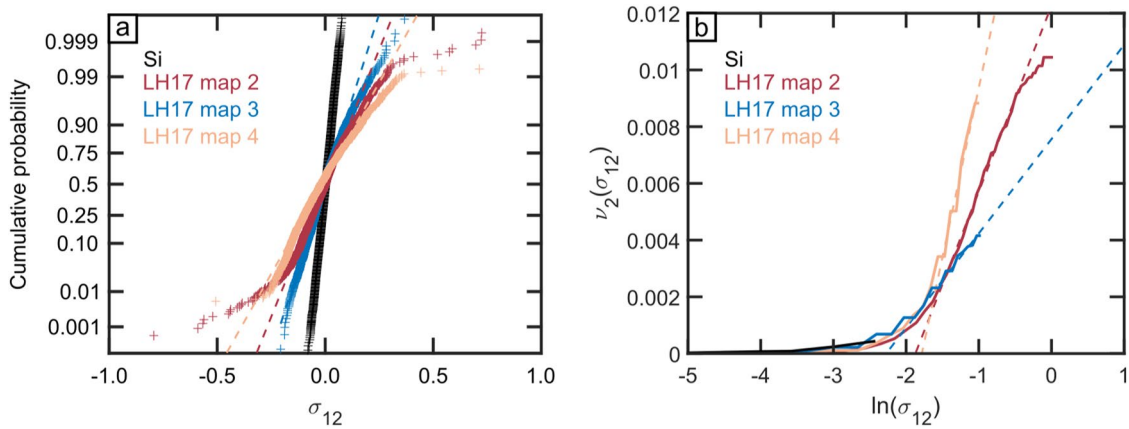

Figure 8. (a) Normal probability plot of normalized in-plane shear stress (σ_{12}) in Maps 2–4 of sample LH17 and the Si standard. The vertical axis is scaled such that a normal distribution plots on a straight line. Dashed lines indicate normal distributions fit the data. (b) Restricted second moment (ν_2) as a function of the in-plane shear stress (σ_{12}) in Maps 2–4 of sample LH17 and the Si standard. The dashed lines provide visual guides to straight lines through the high-stress portions of the datasets.

Tayin, and Fanjah massifs. This consistency suggests that the dislocation content of our samples is likely typical of the basal peridotites along the length of the ophiolite.

The HR-EBSD maps of GND density provide additional constraints on the dislocation types contributing to various structures. In the largest HR-EBSD map of sample LH17, Map 1, subgrain boundaries composed of (001)[100] edge dislocations are particularly abundant (Figure 4), consistent with common misorientation axes parallel to [010] in the conventional EBSD data (Figure 2). Map 2 contains linear structures composed of multiple dislocation types, including prominent slip bands of (010)[001] edge dislocations (Figure 5). Maps 3 and 4 contain a variety of dislocation types with predominantly [001] and [100] Burgers vectors, respectively (Figures 6 and 7). Overall, the EBSD and HR-EBSD results demonstrate that several types of dislocation were active during deformation, forming structures that include subgrain boundaries (e.g., Figures 4 and 7), slip bands (Figure 5), and more broad arrays of GNDs (e.g., (010)[100] edge dislocations in Figure 7).

The densities of decorated dislocations (Figure 3) provide a new estimate of the differential stress applied to samples LH18, LH17, and LH28, which span distances up to approximately 300 m structurally above the metamorphic sole (Figure 1). Total dislocation densities on the order of 10^{12} m^{-2} in each of these samples (Figure 3) suggest macroscopic average differential stresses on the order of 100 MPa (Karato and Jung, 2003). This estimated value is higher than stresses of approximately 20 MPa estimated based on the sizes of subgrains across five of the samples (Ambrose et al., 2018; Goddard et al., 2020), including those used to estimate dislocation density. However, available dislocation-density paleopiezometers are calibrated based on steady-state creep but it is unclear whether the dislocation densities in our samples were set during steady-state or transient creep. If the stress estimate based on dislocation density is accurate then the contrasting estimates suggest temporal heterogeneity in the stresses applied to the peridotites. However, it is difficult to determine whether the different stress magnitudes were applied over a short time interval in a single setting (e.g., stress variation over the seismic cycle on the shallower, frictional fault) or over a more protracted interval of the overall history of the rocks (e.g., deformation at progressively lower temperatures and higher stresses as the rocks were exhumed).

We note that densities of decorated dislocations on the order of 10^{12} m^{-2} are not incompatible with higher apparent densities of GNDs, $\lesssim 10^{14}$ m^{-2}, in the HR-EBSD datasets. The densities of decorated dislocations are estimated from the 'free' dislocations in subgrain interiors and are at or below the noise level (which depends on crystal orientation and step size) in the HR-EBSD data (Wallis et al., 2016). Therefore, the apparent GND densities in some portions of the subgrain interiors (blue regions in the maps of *total* GND density in Figures 4–7) result from measurement noise that obscures the low dislocation densities, whereas regions of elevated GND density stand out above the noise. Moreover, HR-EBSD measurements of GND density, being based on lattice curvature, can also reveal dislocations that did not thread to the specimen surface during oxidation (Wallis et al., 2016).

The distributions of decorated dislocations (Figure 3) indicate that long-range dislocation interactions contributed to the organization of the microstructure. In several instances, the dislocations are organized into bands

with high dislocation densities separated by bands with lower dislocation densities (Figures 3a, 3d, and 3e). The wavelengths of this alternation are on the order of 10 μm. Whilst decoration reveals variations in total dislocation density, comparable bands are also evident in the maps of GND density (Figures 5 and 6). This microstructural organization implies that dislocation interactions were significant across the length scales over which dislocation density fluctuates (Montagnat et al., 2006; Wallis et al., 2017). The dislocations are not organized in entirely two-dimensional slip bands as they would be if their distribution was controlled entirely by the source distribution and nor are they randomly distributed as they would be if they did not interact (Montagnat et al., 2006). Instead, they are organized into broader bands and the sign of the dislocations within those bands commonly alternates between the bands (Figures 5 and 6). This alternation reduces the long-range stresses and associated stored energy relative to a monotonically curved lattice.

4.2. Cause of Residual Stress Heterogeneity

Several lines of evidence strongly indicate that the stress heterogeneity revealed by HR-EBSD (Figures 5–7) is generated by dislocations. Visual comparisons demonstrate an obvious spatial correlation between the GND density and stress heterogeneity (Figures 5–7). Moreover, the characteristics of the probability distribution of σ_{12} are diagnostic of the stress field of a population of dislocations (Figure 8). Unlike the data from the undeformed Si control sample, the data from Maps 2–4 of sample LH17 exhibit significantly broader distributions and, notably, depart from a normal distribution at stress magnitudes greater than approximately 150 MPa (Figure 8a). These high-stress 'tails' to the distributions are typical of the stress fields of populations of dislocations in a wide range of materials, including Cu, InAlN, and steel (Jiang et al., 2013; Kalácska et al., 2017; Wilkinson et al., 2014). These high-stress data also fall on straight lines on the plot of the restricted second moment as a function of $\ln(\sigma_{12})$ (Figure 8b), indicating that the stress fields exhibit the $P(\sigma) \propto |\sigma|^{-3}$ form (Equations 1 and 2) expected of a population of dislocations (Kalácska et al., 2017; Wilkinson et al., 2014). The departure below the straight line at stresses >650 MPa, evident in the data from Map 2, is also typical of stress fields of dislocations measured by HR-EBSD and is interpreted to be due to averaging out of the highest stresses adjacent to dislocation cores over the finite source regions of the diffraction patterns illuminated by the electron beam (Kalácska et al., 2017).

The relationships between GNDs and their stress fields in sample LH17 are closely comparable to those exhibited by samples deformed in laboratory experiments. In previous studies, several characteristics have been broadly consistent among single crystals and aggregates of olivine deformed in experiments at room temperature or temperatures in the range 1000–1250°C, including (a) spatial correlation between regions of elevated GND density and high-stress magnitudes, (b) typical length scales of variation in GND density and stress magnitude on the order of 1–10 μm, (c) high-stress tails to the probability distributions of σ_{12} that follow a $P(\sigma) \propto |\sigma|^{-3}$ relationship, and (d) the occurrence in single crystals of bands of elevated GND density aligned parallel to the trace of the slip plane indicating the presence of slip bands (Wallis et al., 2017, 2020; Wallis, Hansen, et al., 2021). Taken together and in combination with associated mechanical data, these characteristics demonstrate that long-range elastic interactions among dislocations control the microstructural organization and transient mechanical behavior across the wide temperature range previously investigated (Hansen et al., 2019, 2021; Kumamoto et al., 2017; Thom et al., 2020; Wallis et al., 2017, 2020; Wallis, Hansen, et al., 2021). Strikingly, sample LH17 also exhibits all of these microstructural characteristics (Figures 3 and 5–8), indicating that long-range elastic interactions among GNDs generate heterogeneous intragranular stress fields in nature as well as experiments. If long-range dislocation interactions are the dominant micromechanical feature in both experiment and nature, then we might expect that the constitutive equations linking dislocation interactions to transient and steady-state behavior in the laboratory also apply to these geological conditions.

For clarity, we emphasize that residual stress heterogeneity is the physical manifestation of long-range dislocation interactions, which generate back stress as an emergent state variable (Hansen et al., 2021; Wallis et al., 2020). It is difficult to infer the magnitude of former back stress directly from observations of stress heterogeneity, but the presence of long-range stress heterogeneity imparted by the dislocations does demonstrate the mechanism by which back stress can emerge.

Furthermore, we note that because the microstructure and micromechanical state that persists during steady-state creep is the end product of evolution that occurred during the preceding transient, observations of material that were either still within the transient or had reached steady-state can both provide information on the processes occurring during the transient. For example, stress heterogeneity and associated back stress accumulate during

the transient but persist at a steady-state (Hansen et al., 2021; Wallis et al., 2020). Therefore, the presence of long-range internal stresses in the rocks from the Oman-UAE ophiolite supports the back-stress model of transient creep, regardless of whether the final phase of deformation recorded by the microstructure and micromechanical fields occurred during a transient or at steady state.

4.3. Implications for Transient Creep of the Upper Mantle

The finding of significant long-range stress heterogeneity imparted by GNDs in olivine from the subduction interface of the Oman-UAE ophiolite implies that elastic interactions among dislocations provide an intragranular contribution to transient creep in natural settings in the same manner as during deformation experiments (Hansen et al., 2019, 2021; Kumamoto et al., 2017; Thom et al., 2020). Specifically, Hansen et al. (2021) analyzed the transient rheological behavior of single crystals of olivine after changes in stress at temperatures of 1250–1300°C. They found that the transient behavior could be well fit by a flow law with a form based on the microphysics of dislocation glide and typically applied to low-temperature plasticity. Importantly, following stress reductions, the samples commonly exhibited time-dependent (i.e., anelastic) reverse strain before transitioning back to creep in the original direction. This behavior implies the existence of back stress due to dislocation interactions that counteract the applied stress, consistent with the behavior of olivine at temperatures <600°C during deformation by low-temperature plasticity (Hansen et al., 2019, 2021; Thom et al., 2020). Based on these observations, Hansen et al. (2021) recalibrated the flow law for low-temperature plasticity formulated by Hansen et al. (2019) to incorporate the constraints provided by their high-temperature experiments, giving

$$\dot{\varepsilon}_{\mathrm{p}} = A\rho \exp\left(-\frac{\Delta F}{\mathrm{R}T}\right) \sinh\left(\frac{\Delta F}{\mathrm{R}T}\frac{\sigma - \sigma_{\mathrm{b}}}{\Sigma}\right) \tag{3}$$

where $\dot{\varepsilon}_{\mathrm{p}}$ is the plastic strain rate, A is a constant with a value of $10^{11.1\pm0.2}$ $\mathrm{m^2 s^{-1}}$, ρ is dislocation density, ΔF is the activation energy of 827 ± 20 kJ/mol, R is the gas constant, T is the temperature, σ is the applied differential stress, σ_{b} is the back stress, and Σ is an effective resistance of the lattice to dislocation glide of 3.1 GPa. Notably, if the back stress exceeds the applied stress, the effective stress, $\sigma - \sigma_{\mathrm{b}}$, will be negative, inducing reverse dislocation glide and a negative strain rate. The evolution of viscosity with time and/or strain can be incorporated into Equation 3 through the evolution of ρ and σ_{b}.

We use the flow law of Hansen et al. (2021) to make an initial assessment of the contribution of dislocation glide to viscosity changes induced by changes in the stress applied to rocks in and around the subduction interface, based on those preserved in the Oman-UAE ophiolite. Specifically, we consider the effects of stress changes imposed on olivine undergoing steady-state creep at a constant initial stress and strain rate. We compare the viscosity immediately after a stress change to the viscosity during steady-state creep prior to the stress change. We note that the full deformation behavior of rocks may be subject to additional effects including grain-boundary processes (Faul & Jackson, 2015), additional deformation mechanisms, and the presence of other minerals and fluids. However, a benefit of Equation 3, which was calibrated with experiments on single crystals, is that it allows us to explore the contribution and effects of intragranular processes in isolation.

To elucidate the basic characteristics of the deformation behavior, we consider two settings within a subduction zone comparable to that preserved in the Oman-UAE ophiolite. For each setting, we compare the viscosity immediately after a stress change to the viscosity immediately before the stress change at constant dislocation density and back stress. The first setting is within the plate-interface shear zone at a temperature of 900°C and pressure of 1,200 MPa (equivalent to approximately 37 km depth), similar to the peak conditions recorded in the metamorphic sole (Cowan et al., 2014). In this case, we assume an applied stress during initial steady-state creep of 20 MPa based on the macroscopic stress inferred to have been applied to the peridotites based on subgrain-size piezometry (Ambrose et al., 2018; Goddard et al., 2020) and explore superimposed stress changes up to ±20 MPa. The second setting is within the far-field asthenosphere at a temperature of 1300°C and pressure of 3,200 MPa (equivalent to approximately 100 km depth). In this case, we assume an applied stress during initial steady-state creep of 1 MPa and explore superimposed stress changes of up to ±1 MPa. For each case, we compute the strain rate and hence viscosity during initial steady-state creep using the flow law for a single crystal deforming by (010)[001] glide (Bai et al., 1991), based on the observation of slip bands of this slip system in sample LH17 and the inference of Hansen et al. (2021) that this slip system may also control the transient behavior of olivine aggregates. Although we use the (010)[001] slip system as an illustration, the same exercise can be performed for

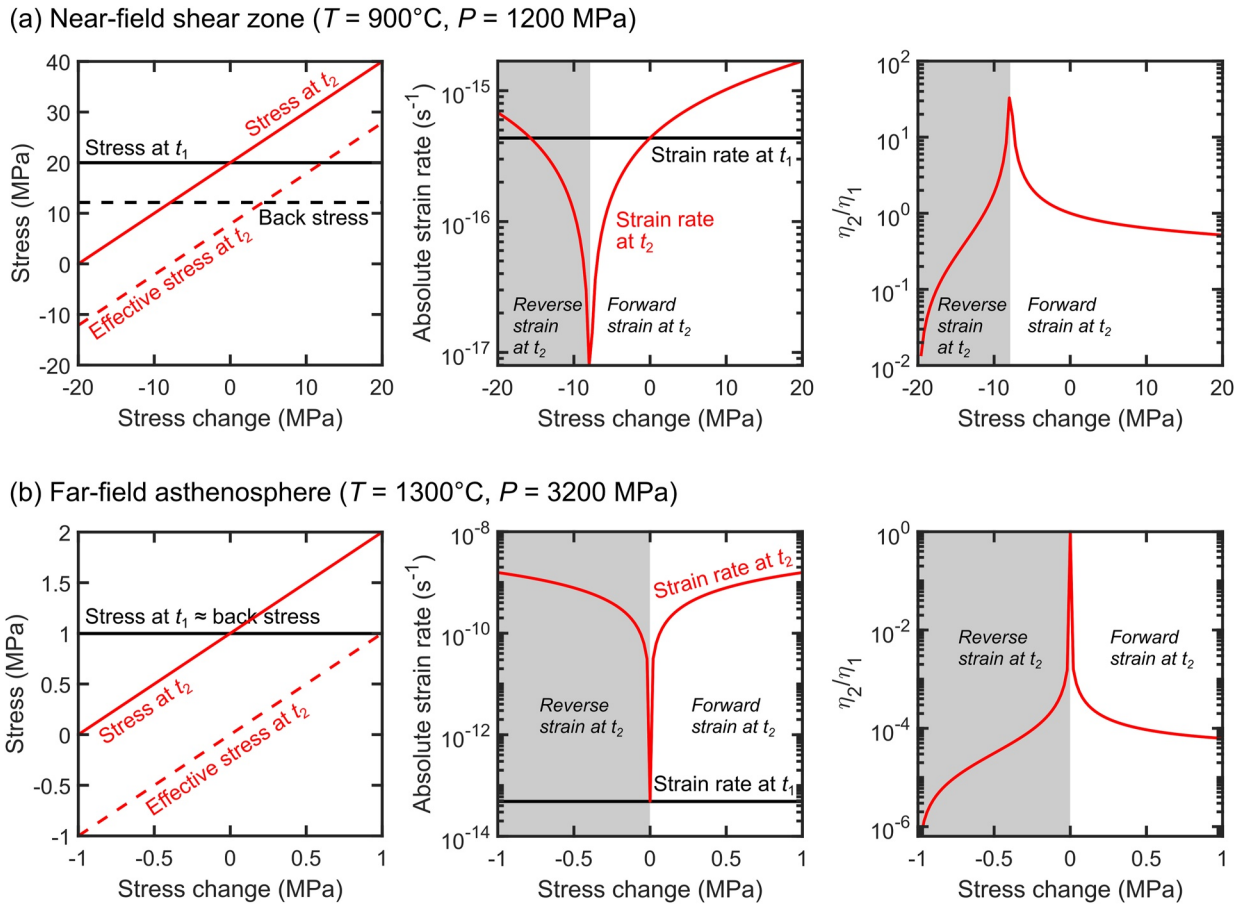

Figure 9. Predicted deformation behavior associated with changes in stress following steady-state creep at constant stress for (a) a shear zone down-dip of the frictional fault within the subduction interface and (b) far-field asthenosphere. The left panel presents the applied stresses before and after the stress change (times t_1 and t_2, respectively), effective stress at t_2, and the back stress, which is the same at both times. The middle panel presents the absolute strain rates at t_1 and t_2. The sense of the strain at t_2 is either the same as at t_1 ('forward strain', no shading) or opposite ('reverse strain', shaded). The right panel presents the ratio of the viscosity after the stress change to that before the stress change (η_2/η_1).

other slip systems. We take the dislocation densities corresponding to the initial applied stresses based on the piezometric relationship of Bai and Kohlstedt (1992) and solve Equation 3 for the back stress required to generate the steady-state strain rate. We assume that during the first increment of plastic deformation after the stress change, prior to any ensuing modification of the dislocation density and arrangement, the dislocation density and back stress will be those established during the preceding steady-state creep. We use these values along with the new applied stress to compute the strain rate, and hence viscosity, after the stress change using Equation 3.

Figures 9a and 9b present the predicted behaviors for the shear-zone and asthenospheric cases, respectively. The effective stress, $\sigma - \sigma_b$, after the stress change can be either positive or negative depending on the relative magnitudes of the preexisting back stress and new applied stress. Correspondingly, the inelastic strain after the stress change either proceeds in the same sense as the prior steady-state creep ('forward strain', unshaded) or in the opposite sense ('reverse strain', shaded), depending on whether the effective stress is positive or negative, respectively. For instance, in the case of the shear zone, the back stress of 12 MPa is 60% of the initial applied stress of 20 MPa (Figure 9a). Therefore, reverse strain is induced when the applied stress is reduced by at least 8 MPa. Thus, a stress change of −8 MPa results in effective stress of 0, a minimum strain rate, and a maximum viscosity. In the case of the shear zone, the ratio of the viscosity after the stress change to that before the stress change (η_2/η_1) is >1 for stress changes in the range −11 to 0 MPa. Stress changes outside that range result in viscosity reductions. The behavior in the case of the asthenosphere is markedly different from that of the shear zone because in the former the back stress approximately equals the initially applied stress and therefore the initial

effective stress is close to zero (Figure 9b). In this case, any stress change results in an increase in absolute strain rate and a reduction in viscosity.

Three overarching characteristics of the behavior are common to both examples (Figures 9a and 9b). First, the minimum viscosity reduction occurs when the effective stress after the stress change is zero, not necessarily when the stress change itself is zero. Second, both cases predict order-of-magnitude changes in viscosity induced by plausible changes in stress. Third, the viscosity reduction depends nonlinearly on effective stress and therefore on the stress change. Whilst the first characteristic cannot yet be compared to data from geodetic studies, the second and third characteristics can. Models of postseismic deformation at subduction zones commonly require the occurrence of transient creep associated with order-of-magnitude reductions in mantle viscosity compared to viscosities associated with the steady-state flow (Broerse et al., 2015; Li et al., 2018; Muto et al., 2019; Pollitz et al., 2006). Similar inferences have also been made based on postseismic deformation following earthquakes in continental interiors (Freed et al., 2012; Guns & Bennett, 2020). In both contexts, the evolution of displacement rates with time over the postseismic interval often indicates that mantle viscosity during transient creep is non-Newtonian, implying that dislocations play a dominant role in generating the deformation (Freed et al., 2006a, 2012; Masuti et al., 2016; Muto et al., 2019). These inferences are broadly consistent with our model predictions.

Recently, transient creep has been modeled using a Burgers rheology, in which the viscous elements have a power-law dependence on stress (Masuti et al., 2016; Muto et al., 2019; Tang et al., 2019, 2020; Weiss et al., 2019). The use of power laws in those analyses focusing on the rheological properties of the mantle is based on the steady-state rheological behavior of olivine observed in deformation experiments (Bai et al., 1991; Durham & Goetze, 1977; Hirth & Kohlstedt, 2003; Keefner et al., 2011). Specifically, some recent analyses of transient creep invoke the concept of stress transfer among soft and hard slip systems to maintain strain compatibility within an aggregate of anisotropic grains (Ashby & Duval, 1985; Karato, 1998; Masuti et al., 2019). In that model, upon an increase in stress, initial deformation occurs in grains oriented such that the softest slip system is subjected to high resolved shear stress. As this initial deformation proceeds, the load is transferred to adjacent grains in which the softest slip system is unfavorably oriented for slip (having lower Schmid factors and lower resolved shear stresses) and harder slip systems are activated instead. This transition in the slip systems that control the bulk strain rate is inferred to result in strain-hardening transient creep.

There are at least two problems with modeling transient creep of olivine based on the stress-transfer model formulated as a non-linear Burgers rheology. The first is that, although a Burgers model can reproduce several first-order phenomenological characteristics of the deformation (i.e., transient creep that transitions to steady-state flow, with potential for anelastic behavior), the form of the system of equations is only loosely linked to the microphysics of dislocation motion. In contrast, both Equation 3 and typical power-law flow laws for steady-state dislocation creep are derived directly from the Orowan equation, which describes dislocation glide in its most fundamental form, by incorporating the dependencies of dislocation density and velocity on variables including stress and temperature (Hansen et al., 2019, 2021; Kohlstedt & Hansen, 2015; Orowan, 1940). This explicit link to the underlying processes is important in validating the physical relevance of model predictions or fitted parameters. Second, it is inappropriate to use power-law flow laws formulated and calibrated for steady-state creep to model non-steady-state behavior. This point is highlighted by the recent experimental results of Hansen et al. (2021), which indicate that the very low strains associated with the onset of transient creep occur by dislocation glide at strain rates that are better fit by Equation 3 than a power-law form typically applied to steady-state flow. We note that some dislocation glide and associated modification of the dislocation density and/or back stress must proceed for stress transfer between grains to ensue. Therefore, it is important to consider the contribution of these intragranular processes to changes in viscosity following changes in stress (e.g., Figure 9) alongside any intergranular stress transfer that may occur during the evolution of viscosity toward steady state.

Our new microstructural and micromechanical evidence, which supports the application of Equation 3 in modeling transient creep, highlights several considerations for such models. As emphasized above, the first-order characteristics of the stress fields of dislocations are broadly similar across a wide temperature range spanning at least 25–1250°C (Figures 5–8; Hansen et al., 2021; Wallis et al., 2017, 2020; Wallis, Hansen, et al., 2021), which supports the use of Equation 3 to model transient creep based on the evolution of back stress across a broad range of geologically relevant conditions. However, the material behavior can vary significantly across conditions due, for instance, to differences in the level of the back stress relative to applied stress at steady state (e.g., Figure 9).

It is therefore important to consider the background stress (Freed et al., 2012; Muto et al., 2019) and back stress (Hansen et al., 2021) at steady state prior to stress changes. The incorporation of Equation 3 into large-scale models of postseismic deformation also requires additional constraints on the kinetics of the evolution of dislocation density and back stress to describe the transition from initial dislocation glide to steady-state creep. The calibration of this evolution is the subject of ongoing work.

5. Conclusions

Olivine within peridotites from the palaeosubduction interface of the Oman-UAE ophiolite preserves heterogeneous dislocation densities with dislocations often organized into bands. The spatial distributions of GNDs correlate with the spatial distributions of heterogeneous residual stresses, in which individual components of the stress tensor vary by hundreds of megapascals over distances of a few micrometers. These spatial correlations, along with characteristic probability distributions of the stresses, indicate that the stresses are imparted by the dislocations and therefore record long-range dislocation interactions. These microstructures and stress fields are highly similar to those generated in recent deformation experiments, in which long-range dislocation interactions were demonstrated to generate kinematic hardening and associated anelastic transient creep. This comparison supports the applicability of a recent experimentally calibrated model for transient creep based on dislocation glide under the influence of back stress. Initial predictions of this model, based on stresses and temperatures relevant to subduction zones, suggest that instantaneous stress changes imposed by earthquakes can generate order-of-magnitude reductions in viscosity that depend non-linearly on the stress change. These characteristics are consistent with inferences based on geodetic observations of postseismic transient creep and raise the possibility that intragranular processes may contribute significantly to the observed behavior.

Data Availability Statement

Data in this paper can be accessed from GFZ Data Services (Wallis, Sep, et al., 2021).

Acknowledgments
We thank Tyler Ambrose for providing the conventional EBSD data and for discussions on the geological context. We thank Mike Searle for conversations on the geology of the ophiolite. This work was supported by the Natural Environment Research Council [grant number NE/M000966/1]; a UK Research and Innovation Future Leaders Fellowship [grant number MR/V021788/1]; the Netherlands Organisation for Scientific Research, User Support Programme Space Research, grant ALWGO.2018.038; and startup funds from Utrecht University.

References

Abramson, E. H., Brown, J. M., Slutsky, L. J., & Zaug, J. (1997). The elastic constants of San Carlos olivine to 17 GPa. *Journal of Geophysical Research: Solid Earth*, *102*, 12253–12263. https://doi.org/10.1029/97jb00682

Agard, P., Yamato, P., Soret, M., Prigent, C., Guillot, S., Plunder, A., et al. (2016). Plate interface rheological switches during subduction infancy: Control on slab penetration and metamorphic sole formation. *Earth and Planetary Science Letters*, *451*, 208–220. https://doi.org/10.1016/j.epsl.2016.06.054

Ambrose, T. K., Wallis, D., Hansen, L. N., Waters, D. J., & Searle, M. P. (2018). Controls on the rheological properties of peridotite at a palaeosubduction interface: A transect across the base of the Oman–UAE ophiolite. *Earth and Planetary Science Letters*, *491*, 193–206. https://doi.org/10.1016/j.epsl.2018.03.027

Andrade, E. N. D. C. (1910). On the viscous flow in metals, and allied phenomena. *Proceedings of the Royal Society A*, *84*, 1–12.

Ashby, M. F., & Duval, P. (1985). The creep of polycrystalline ice. *Cold Regions Science and Technology*, *11*, 285–300. https://doi.org/10.1016/0165-232x(85)90052-7

Bai, Q., & Kohlstedt, D. L. (1992). High-temperature creep of olivine single crystals, 2. dislocation structures. *Tectonophysics*, *206*, 1–29. https://doi.org/10.1016/0040-1951(92)90365-d

Bai, Q., Mackwell, S. J., & Kohlstedt, D. L. (1991). High-temperature creep of olivine single crystals 1. Mechanical results for buffered samples. *Journal of Geophysical Research: Solid Earth*, *96*, 2441–2463. https://doi.org/10.1029/90jb01723

Bayley, C. J., Brekelmans, W. A. M., & Geers, M. G. D. (2006). A comparison of dislocation induced back stress formulations in strain gradient crystal plasticity. *International Journal of Solids and Structures*, *43*, 7268–7286. https://doi.org/10.1016/j.ijsolstr.2006.05.011

Birch, J. M., & Wilshire, B. (1974). The effect of stress changes during creep of single-and polycrystalline MgO. *Philosophical Magazine*, *30*, 1023–1031. https://doi.org/10.1080/14786437408207255

Britton, T. B., Jiang, J., Guo, Y., Vilalta-Clemente, A., Wallis, D., Hansen, L. N., et al. (2016). Tutorial: Crystal orientations and EBSD — or which way is up? *Materials Characterization*, *117*, 113–126. https://doi.org/10.1016/j.matchar.2016.04.008

Britton, T. B., & Wilkinson, A. J. (2011). Measurement of residual elastic strain and lattice rotations with high resolution electron backscatter diffraction. *Ultramicroscopy*, *111*, 1395–1404. https://doi.org/10.1016/j.ultramic.2011.05.007

Britton, T. B., & Wilkinson, A. J. (2012). High resolution electron backscatter diffraction measurements of elastic strain variations in the presence of larger lattice rotations. *Ultramicroscopy*, *114*, 82–95. https://doi.org/10.1016/j.ultramic.2012.01.004

Broerse, T., Riva, R., Simons, W., Govers, R., & Vermeersen, B. (2015). Postseismic GRACE and GPS observations indicate a rheology contrast above and below the Sumatra slab. *Journal of Geophysical Research: Solid Earth*, *120*, 5343–5361. https://doi.org/10.1002/2015jb011951

Campbell, L. R., & Menegon, L. (2019). Transient high strain rate during localized viscous creep in the dry lower continental crust (Lofoten, Norway). *Journal of Geophysical Research: Solid Earth*, *124*, 10240–10260. https://doi.org/10.1029/2019jb018052

Chopra, P. N. (1997). High-temperature transient creep in olivine rocks. *Tectonophysics*, *279*, 93–111. https://doi.org/10.1016/s0040-1951(97)00134-0

Cooper, R. F., Stone, D. S., & Plookphol, T. (2016). Load relaxation of olivine single crystals. *Journal of Geophysical Research: Solid Earth*, *121*, 7193–7210. https://doi.org/10.1002/2016jb013425

Cowan, R. J., Searle, M. P., & Waters, D. J. (2014). Structure of the metamorphic sole to the Oman ophiolite, Sumeini window and Wadi Tayyin: Implications for ophiolite obduction processes. *Geological Society, London, Special Publications*, *392*, 155–175. https://doi.org/10.1144/sp392.8

Csikor, F. F., & Groma, I. (2004). Probability distribution of internal stress in relaxed dislocation systems. *Physical Review B*, *70*, 064106.https://doi.org/10.1103/physrevb.70.064106

De Bresser, J. H. P. (1996). Steady state dislocation densities in experimentally deformed calcite materials: Single crystals versus polycrystals. *Journal of Geophysical Research*, *101*, 22189–22201. https://doi.org/10.1029/96jb01759

Durham, W. B., Froidevaux, C., & Jaoul, O. (1979). Transient and steady-state creep of pure forsterite at low stress. *Physics of the Earth and Planetary Interiors*, *19*, 263–274. https://doi.org/10.1016/0031-9201(79)90027-x

Durham, W. B., & Goetze, C. (1977). Plastic flow of oriented single crystals of olivine: 1. Mechanical data. *Journal of Geophysical Research*, *82*, 5737–5753. https://doi.org/10.1029/jb082i036p05737

Durham, W. B., Goetze, C., & Blake, B. (1977). Plastic flow of oriented single crystals of olivine: 2. Observations and interpretations of the dislocation structures. *Journal of Geophysical Research*, *82*, 5755–5770. https://doi.org/10.1029/jb082i036p05755

Duval, P., Ashby, M. F., & Anderman, I. (1983). Rate-controlling processes in the creep of polycrystalline ice. The *Journal of Physical Chemistry A*, *87*, 4066–4074. https://doi.org/10.1021/j100244a014

Farrant, A., Ellison, R. A., Thomas, R. J., Goodenough, K. M., Arkley, S. L. B., Burke, H. F., et al. (2012). *Geological map of the United Arab Emirates*.

Faul, U., & Jackson, I. (2015). Transient creep and strain energy dissipation: An experimental perspective. *Annual Review of Earth and Planetary Sciences*, *43*, 541–569. https://doi.org/10.1146/annurev-earth-060313-054732

Freed, A. M. (2005). Earthquake triggering by static, dynamic, and postseismic stress transfer. *Annual Review of Earth and Planetary Sciences*, *33*, 335–367. https://doi.org/10.1146/annurev.earth.33.092203.122505

Freed, A. M., Bürgmann, R., Calais, E., & Freymueller, J. (2006). Stress-dependent power-law flow in the upper mantle following the 2002 Denali, Alaska, earthquake. *Earth and Planetary Science Letters*, *252*, 481–489. https://doi.org/10.1016/j.epsl.2006.10.011

Freed, A. M., Bürgmann, R., Calais, E., Freymueller, J., & Hreinsdóttir, S. (2006). Implications of deformation following the 2002 Denali, Alaska, earthquake for postseismic relaxation processes and lithospheric rheology. *Journal of Geophysical Research: Solid Earth*, *111*, B01401. https://doi.org/10.1029/2005jb003894

Freed, A. M., Hirth, G., & Behn, M. D. (2012). Using short-term postseismic displacements to infer the ambient deformation conditions of the upper mantle. *Journal of Geophysical Research: Solid Earth*, *117*, B01409. https://doi.org/10.1029/2011jb008562

Gangi, A. F. (1983). Transient and steady-state deformation of synthetic rocksalt. *Tectonophysics*, *91*, 137–156. https://doi.org/10.1016/0040-1951(83)90062-8

Goddard, R. M., Hansen, L. N., Wallis, D., Stipp, M., Holyoke, C. W., Kumamoto, K. M., & Kohlstedt, D. L. (2020). A subgrain-size piezometer calibrated for EBSD. *Geophysical Research Letters*, *47*, e2020GL09005. https://doi.org/10.1029/2020gl090056

Groma, I., & Bakó, B. (1998). Probability distribution of internal stresses in parallel straight dislocation systems. *Physical Review B*, *58*, 2969–2974. https://doi.org/10.1103/physrevb.58.2969

Guns, K. A., & Bennett, R. A. (2020). Assessing long-term postseismic transients from GPS time series in Southern California. *Journal of Geophysical Research: Solid Earth*, *125*, e2019JB018670. https://doi.org/10.1029/2019jb018670

Hansen, L. N., Kumamoto, K. M., Thom, C. A., Wallis, D., Durham, W. B., Goldsby, D. L., et al. (2019). Low-temperature plasticity in olivine: Grain size, strain hardening, and the strength of the lithosphere. *Journal of Geophysical Research: Solid Earth*, *124*, 5427–5449. https://doi.org/10.1029/2018jb016736

Hansen, L., Wallis, D., Breithaupt, T., Thom, C., & Kempton, I. (2021). Dislocation creep of olivine: Backstress evolution controls transient creep at high temperatures. *Journal of Geophysical Research: Solid Earth*, *126*, e2020JB021325. https://doi.org/10.1029/2020jb021325

Hanson, D. R., & Spetzler, H. A. (1994). Transient creep in natural and synthetic, iron-bearing olivine single crystals: Mechanical results and dislocation microstructures. *Tectonophysics*, *235*, 293–315. https://doi.org/10.1016/0040-1951(94)90191-0

Hirth, G., & Kohlstedt, D. (2003). Rheology of the upper mantle and the mantle wedge: A view from the experimentalists. In J. Eiler (Ed.), *Inside the subduction factory. Geophysical Monograph Series 38* (pp. 83–105). : American Geophysical Union. https://doi.org/10.1029/138gm06

Holtzman, B. K., Chrysochoos, A., & Daridon, L. (2018). A thermomechanical framework for analysis of microstructural evolution: Application to olivine rocks at high temperature. *Journal of Geophysical Research: Solid Earth*, *123*, 8474–8507. https://doi.org/10.1029/2018jb015613

Jiang, J., Benjamin Britton, T., & Wilkinson, A. J. (2013). Mapping type III intragranular residual stress distributions in deformed copper polycrystals. *Acta Materialia*, *61*, 5895–5904. https://doi.org/10.1016/j.actamat.2013.06.038

Jung, H., Katayama, I., Jiang, Z., Hiraga, T., & Karato, S. (2006). Effect of water and stress on the lattice-preferred orientation of olivine. *Tectonophysics*, *421*, 1–22. https://doi.org/10.1016/j.tecto.2006.02.011

Kalácska, S., Groma, I., Borbély, A., & Ispánovity, P. D. (2017). Comparison of the dislocation density obtained by HR-EBSD and X-ray profile analysis. *Applied PhysicsLetters*,*110*, 091912.

Karato, S.-I. (1998). Micro-physics of post glacial rebound. *In:* In P. Wu (Ed.), *Dynamics of the Ice Age Earth: A modern Perspective, GeoResearch Forum* (pp. 351–364). : Trans Tech Publications

Karato, S.-I., & Jung, H. (2003). Effects of pressure on high-temperature dislocation creep in olivine. *Philosophical Magazine*, *83*, 401–414. https://doi.org/10.1080/0141861021000025829

Keefner, J. W., Mackwell, S. J., Kohlstedt, D. L., & Heidelbach, F. (2011). Dependence of dislocation creep of dunite on oxygen fugacity: Implications for viscosity variations in Earth's mantle. *Journal of Geophysical Research: Solid Earth*, *116*, B05201.https://doi.org/10.1029/2010jb007748

de Kloe, R., Drury, M., & Farrer, J. K. (2002). Determination of activated slip systems in experimentally deformed olivine-orthopyroxene polycrystals using EBSD. *Microscopy and Microanalysis*, *8*, 680–681. https://doi.org/10.1017/s1431927602106404

Kohlstedt, K. L., Goetze, C., Durham, W. B., & Vander Sande, J. (1976). New technique for decorating dislocations in olivine. *Science*, *191*, 1045–1046. https://doi.org/10.1126/science.191.4231.1045

Kohlstedt, D. L., & Hansen, L. N. (2015). Constitutive equations, rheological behavior, and viscosity of rocks. In G. Schubert (Ed.), *Treatise on Geophysics 2* (pp. 441–472). : Elsevier. https://doi.org/10.1016/b978-0-444-53802-4.00042-7

Kumamoto, K. M., Thom, C. A., Wallis, D., Hansen, L. N., Armstrong, D. E. J., Warren, J. M., et al. (2017). Size effects resolve discrepancies in 40 years of work on low-temperature plasticity in olivine. *Science Advances*, *3*, e1701338. https://doi.org/10.1126/sciadv.1701338

Li, S., Bedford, J., Moreno, M., Barnhard, W. D., Rosenau, M., & Oncken, O. (2018). Spatiotemporal variation of mantle viscosity and the presence of Cratonic mantle inferred from 8 Years of postseismic deformation following the 2010 Maule, Chile, earthquake. *Geochemistry, Geophysics, Geosystems*, *19*, 3272–3285. https://doi.org/10.1029/2018gc007645

Linckens, J., Herwegh, M., Müntener, O., & Mercolli, I. (2011). Evolution of a polymineralic mantle shear zone and the role of second phases in the localization of deformation. *Journal of Geophysical Research: Solid Earth*, *116*, B06210. https://doi.org/10.1029/2010jb008119
MacLeod, C. J., Johan Lissenberg, C., & Bibby, L. E. (2013). "Moist MORB" axial magmatism in the Oman ophiolite: The evidence against a mid-ocean ridge origin. *Geology*, *41*, 459–462. https://doi.org/10.1130/g33904.1
Masuti, S., Barbot, S. D., Karato, S.-I., Feng, L., & Banerjee, P. (2016). Upper-mantle water stratification inferred from observations of the 2012 Indian Ocean earthquake. *Nature*, *538*, 373–377. https://doi.org/10.1038/nature19783
Masuti, S., Karato, S.-I., Girard, J., & Barbot, S. D. (2019). Anisotropic high-temperature creep in hydrous olivine single crystals and its geodynamic implications. *Physics of the Earth and Planetary Interiors*, *290*, 1–9. https://doi.org/10.1016/j.pepi.2019.03.002
Matysiak, A. K., & Trepmann, C. A. (2012). Crystal–plastic deformation and recrystallization of peridotite controlled by the seismic cycle. *Tectonophysics*, *530–531*, 111–127. https://doi.org/10.1016/j.tecto.2011.11.029
McLaren, A. C., D, F. G. J., & Gerretsen, J. (1989). Dislocation nucleation and multiplication in synthetic quartz: Relevance to water weakening. *Physics and Chemistry of Minerals*, *16*, 465–482. https://doi.org/10.1007/bf00197016
Michibayashi, K., & Mainprice, D. (2004). The role of pre-existing mechanical anisotropy on shear zone development within oceanic mantle lithosphere: An example from the Oman ophiolite. *Journal of Petrology*, *45*, 405–414. https://doi.org/10.1093/petrology/egg099
Montagnat, M., Weiss, J., Chevy, J., Duval, P., Brunjail, H., Bastie, P., & Gil Sevillano, J. (2006). The heterogeneous nature of slip in ice single crystals deformed under torsion. *Philosophical Magazine*, *86*, 4259–4270. https://doi.org/10.1080/14786430500452602
Moore, J. D. P., Yu, H., Tang, C.-H., Wang, T., Barbot, S., Peng, D., et al. (2017). Imaging the distribution of transient viscosity after the 2016 7.1 Kumamoto earthquake. *Science*, *356*, 163–167. https://doi.org/10.1126/science.aal3422
Muto, J., Moore, J. D. P., Barbot, S., Iinuma, T., Ohta, Y., & Iwamori, H. (2019). Coupled afterslip and transient mantle flow after the 2011 Tohoku earthquake. *Science Advances*, *5*, eaaw1164. https://doi.org/10.1126/sciadv.aaw1164
Nüchter, J.-A., & Ellis, S. (2011). Mid-crustal controls on episodic stress-field rotation around major reverse, normal and strike-slip faults. *Geological Society, London, Special Publications*, *359*, 187–201.
Orlová, A., & Čadek, J. (1986). Dislocation structure in the high temperature creep of metals and solid solution alloys: A review. *Materials Science and Engineering*, *77*, 1–18.
Orlová, A., Pahutová, M., & Čadek, J. (1972). Dislocation structure and applied, effective and internal stress in high-temperature creep of alpha iron. *Philosophical Magazine*, *25*, 865–877.
Orowan, E. (1940). Problems of plastic gliding. *Proceedings of the Physical Society*, *52*, 8–22. https://doi.org/10.1088/0959-5309/52/1/303
Pollitz, F. F., Bürgmann, R., & Banerjee, P. (2006). Post-seismic relaxation following the great 2004 Sumatra-Andaman earthquake on a compressible self-gravitating Earth. *Geophysical Journal International*, *167*, 397–420. https://doi.org/10.1111/j.1365-246x.2006.03018.x
Post, R. L. (1977). High-temperature creep of Mt. Burnet dunite. *Tectonophysics*, *42*, 75–110. https://doi.org/10.1016/0040-1951(77)90162-7
Prigent, C., Agard, P., Guillot, S., Godard, M., & Dubacq, B. (2018). Mantle wedge (de)formation during subduction infancy: Evidence from the base of the semail ophiolitic mantle. *Journal of Petrology*, *59*, 2061–2092. https://doi.org/10.1093/petrology/egy090
Prigent, C., Guillot, S., Agard, P., & Ildefonse, B. (2018). Fluid-assisted deformation and strain localization in the cooling mantle wedge of a Young subduction zone (Semail Ophiolite). *Journal of Geophysical Research: Solid Earth*, *123*, 7529–7549. https://doi.org/10.1029/2018jb015492
Rioux, M., Garber, J., Bauer, A., Bowring, S., Searle, M., Kelemen, P., & Hacker, B. (2016). Synchronous formation of the metamorphic sole and igneous crust of the Semail ophiolite: New constraints on the tectonic evolution during ophiolite formation from high-precision U–Pb zircon geochronology. *Earth and Planetary Science Letters*, *451*, 185–195. https://doi.org/10.1016/j.epsl.2016.06.051
Savage, J. C., Svarc, J. L., & Yu, S.-B. (2005). Postseismic relaxation and transient creep. *Journal of Geophysical Research: Solid Earth*, *110*, B11402. https://doi.org/10.1029/2005jb003687
Searle, M. P., & Malpas, J. (1980). Structure and metamorphism of rocks beneath the Semail ophiolite of Oman and their significance in ophiolite obduction. *Transactions of the Royal Society of Edinburgh Earth Sciences*, *71*, 247–262. https://doi.org/10.1017/s0263593300013614
Smith, C. L. (1948). A theory of transient creep in metals. *Proceedings of the Physical Society*, *61*, 201–205. https://doi.org/10.1088/0959-5309/61/3/301
Smith, B. K., & Carpenter, F. O. (1987). Transient creep in orthosilicates. *Physics of the Earth and Planetary Interiors*, *49*, 314–324. https://doi.org/10.1016/0031-9201(87)90033-1
Tang, C.-H., Barbot, S., Hsu, Y.-J., & Wu, Y.-M. (2020). Heterogeneous power-law flow with transient creep in Southern California following the 2010 El Mayor-Cucapah Earthquake. *Journal of Geophysical Research: Solid Earth*, *125*, e2020JB019740. https://doi.org/10.1029/2020jb019740
Tang, C.-H., Hsu, Y.-J., Barbot, S., Moore, J. D. P., & Chang, W.-L. (2019). Lower-crustal rheology and thermal gradient in the Taiwan orogenic belt illuminated by the 1999 Chi-Chi earthquake. *Science Advances*, *5*, eaav3287. https://doi.org/10.1126/sciadv.aav3287
Thatcher, W. (1983). Nonlinear strain buildup and the earthquake cycle on the San Andreas Fault. *Journal of Geophysical Research*, *88*, 5893–5902. https://doi.org/10.1029/jb088ib07p05893
Thom, C., Hansen, L., Goldsby, D., & Kumamoto, K. (2020). Backstress from dislocation interactions quantified by nanoindentation load-drop experiments. *EarthArXiv*. https://doi.org/10.31223/x5z88w
Wallis, D., Hansen, L. N., Ben Britton, T., & Wilkinson, A. J. (2016). Geometrically necessary dislocation densities in olivine obtained using high-angular resolution electron backscatter diffraction. *Ultramicroscopy*, *168*, 34–45. https://doi.org/10.1016/j.ultramic.2016.06.002
Wallis, D., Hansen, L. N., Ben Britton, T., & Wilkinson, A. J. (2017). Dislocation interactions in olivine revealed by HR-EBSD. *Journal of Geophysical Research: Solid Earth*, *122*, 7659–7678. https://doi.org/10.1002/2017jb014513
Wallis, D., Hansen, L. N., Britton, T. B., & Wilkinson, A. J. (2019). High-angular resolution electron backscatter diffraction as a new tool for mapping lattice distortion in geological minerals. *Journal of Geophysical Research: Solid Earth*, *124*, 6337–6358. https://doi.org/10.1029/2019jb017867
Wallis, D., Hansen, L. N., Kumamoto, K. M., Thom, C. A., Plümper, O., Ohl, M., et al. (2020). Dislocation interactions during low-temperature plasticity of olivine and their impact on the evolution of lithospheric strength. *Earth and Planetary Science Letters*, *543*, 116349. https://doi.org/10.1016/j.epsl.2020.116349
Wallis, D., Hansen, L., Wilkinson, A. J., & Lebensohn, R. A. (2021). Dislocation interactions in olivine control postseismic creep of the upper mantle. *Nature Communications*, *12*, 3496. https://doi.org/10.1038/s41467-021-23633-8
Wallis, D., Sep, M., & Hansen, L. N. (2021). Decorated dislocations and (HR-)EBSD data from olivine of the Oman-UAE ophiolite. *GFZ Data Services*. https://doi.org/10.5880/fidgeo.2021.050
Weckert, E. & Blum, W. (1985). Transient creep of an Al-5at%Mg solid solution. Strength of Metals and Alloys (ISCMA 7), 773–778.
Weiss, J. R., Qiu, Q., Barbot, S., Wright, T. J., Foster, J. H., Saunders, A., et al. (2019). Illuminating subduction zone rheological properties in the wake of a giant earthquake. *Science Advances*, *5*, eaax6720. https://doi.org/10.1126/sciadv.aax6720

Wilkinson, A. J., Meaden, G., & Dingley, D. J. (2006). High-resolution elastic strain measurement from electron backscatter diffraction patterns: New levels of sensitivity. *Ultramicroscopy*, *106*, 307–313. https://doi.org/10.1016/j.ultramic.2005.10.001

Wilkinson, A. J., Tarleton, E., Vilalta-Clemente, A., Jiang, J., Benjamin Britton, T., & Collins, D. M. (2014). Measurement of probability distributions for internal stresses in dislocated crystals. *Applied Physics Letters*, *105*, 181907. https://doi.org/10.1063/1.4901219

Wyatt, O. H. (1951). Transient creep in pure metals. *Nature*, *167*. https://doi.org/10.1038/167866a0